



University  
ofGlasgow

# Experimental observations of droplet formation and polydispersity in T-junction microfluidic devices operating under pressure-driven flow

Aaron Delahanty  
BSc Mechanical Engineering

School of Engineering  
College of Science and Engineering  
University of Glasgow

Submitted in fulfillment of the requirements for the Degree of  
*Master of Science*

2016

## **Acknowledgements**

I would like to express my gratitude to Thomas Franke and his group for their generosity of time, patience, and guidance. Thank you to Matthew Tang of Hong Kong University for his contribution of the measurement of applicable interfacial tensions. I would also like to thank the international community of University of Glasgow as a whole for the inclusivity, support, and provided laughs.

## Abstract

Microfluidic devices generally require precise control of fluid flowrates in order to reliably perform their various functions. Here a pressure-driven flow controller (PDFC) is developed and characterized for use as a flow provider for droplet-makers and as a tool for further microfluidics-based research.

The PDFC is first designed, manufactured and characterized prior to being applied to the study of droplet formation. Previously, droplet-makers that utilize volumetric flow control have been used to define the relationship between continuous and discontinuous phase flowrates and the resulting droplet parameters and flow regimes. Here, experimentation is conducted investigating the same droplet formation behavior but as observed in a system driven by pressure-based flow in a T-junction droplet generating device.

The PDFC system was characterized to show pressure control ranging from 0 to 1000mbar with 4 discreetly controlled channels capable of  $\pm 1$  mbar accuracy with a measured signal standard deviation of 0.25 mbar and signal to noise ratio of 400. The PDFC was then applied to microfluidic droplet production. Here, for the first time the transition from dripping to squeezing droplet formation regimes is experimentally documented in a pressure-driven flow system. The resulting droplets show high monodispersity with less than 1% coefficient of variation in droplet length in all measured populations.

# Contents

<b>1</b>	<b>Introduction</b>	<b>1</b>
<b>2</b>	<b>System Development</b>	<b>3</b>
2.1	Design . . . . .	3
2.2	Characterization . . . . .	9
<b>3</b>	<b>Background Theory</b>	<b>12</b>
3.1	Fluid Dynamics at the Microscale . . . . .	12
3.2	Droplet Microfluidics Overview . . . . .	13
3.3	Determining System Flowrates . . . . .	15
<b>4</b>	<b>System Application - Droplet Microluidics</b>	<b>20</b>
4.1	Aims . . . . .	20
4.2	Methods . . . . .	20
4.2.1	Device Generation . . . . .	20
4.2.2	Reagents . . . . .	21
4.2.3	Experimental Procedure . . . . .	21
4.2.4	Analysis of Collected Data . . . . .	21
4.3	Results . . . . .	22
4.3.1	Regime Transition . . . . .	22
4.3.2	Droplet Polydispersity . . . . .	25
4.4	Discussion . . . . .	27
4.4.1	Droplet Regime Transition . . . . .	27
4.4.2	Droplet Polydispersity . . . . .	30
<b>5</b>	<b>Conclusions</b>	<b>31</b>
5.1	Areas of Further Investigation . . . . .	31
5.1.1	Improvement of Time Response . . . . .	31
5.1.2	Addition of External Triggers . . . . .	31

5.2	Achievements . . . . .	32
5.2.1	Device Development . . . . .	32
5.2.2	Application to Droplet Formation . . . . .	32
<b>A</b>	<b>Arduino Code</b>	<b>33</b>
<b>B</b>	<b>LabVIEW VI</b>	<b>37</b>
<b>C</b>	<b>Supplementary Statistics</b>	<b>40</b>
	<b>Bibliography</b>	<b>43</b>

# List of Figures

2.1	Image of Packaged PDFC . . . . .	5
2.2	Pneumatic Schematic of PDFC channel . . . . .	6
2.3	LabVIEW write command . . . . .	7
2.4	System Overview of the PDFC . . . . .	8
2.5	PDFC time response . . . . .	10
2.6	PDFC accuracy and inter-channel variation . . . . .	11
3.1	Hydraulic Resistance of System . . . . .	16
3.2	Pressure Balance at no-flow condition. . . . .	18
4.1	Custom ImageJ Droplet Analysis Script . . . . .	22
4.2	Droplet Length as a Function of Applied Control Pressure Ratio . . . . .	23
4.3	Droplet length as a function of Capillary number across squeezing and dripping regimes . . . . .	24
4.4	Polydispersity . . . . .	25
4.5	Critical capillary number as a function of continuous phase applied pressure . . . . .	28
4.6	Droplet Length as a function of Corrected Capillary Number . . . . .	29
B.1	LabVIEW Frontend . . . . .	37
B.2	LabVIEW Backend 1 . . . . .	38
B.3	LabVIEW Backend 2 . . . . .	38
B.4	LabVIEW Backend 3 . . . . .	39
B.5	LabVIEW Backend 4 . . . . .	39
C.1	Linear Regression Statistical Summary . . . . .	40
C.2	Polydispersity at CA = 0.014 . . . . .	41
C.3	Polydispersity at CA = 0.018 . . . . .	42

# Chapter 1

## Introduction

The study of microfluidics requires by definition generation of fluid flow. In research and experimental environments syringe pumps are commonly used as flow providers [8]. They offer the advantage of being capable of directly controlling the rate of flow in units of volume per time. Furthermore, programmable syringe pumps have been developed that allow for modulation of flowrate as a function of time. An alternative to syringe pump systems is pressure-driven flow in which precision regulated compressed gas is used to pressurize fluid-filled reagent reservoirs, which in turn drives flow through small diameter tubing and subsequently any applicable microfluidic device. A custom developed pressure-driven flow system may offer advantages such as increased flow stability, capability to support high numbers of parallel flow channels, and flowrate modulation response time [4, 16]. This project focus on the development of such a system, herein referred to as a Pressure Driven Flow Controller (PDFC).

One application of the system is the formation of micro-droplets. Micro-droplets are generally an aqueous vessel contained within an oil carrier, whose biological applications span DNA analysis, protein crystallization, and cell encapsulation. Furthermore, highly precise fluidic operations can be performed on the microscale including mixing, merging, and splitting [10]. The method and technology surrounding droplet production is relatively mature, first demonstrated by Thorson *et al.* in 2001 [22]. However, droplet production using pressure-driven flow is relatively uncharacterized and has been identified as an area in need of further investigation [8].

The work documented here can be divided into two primary categories. First, the PDFC system is designed, built, and characterized. Secondly, the developed device is put to use to characterize micro-droplet formation in T-junction geometry operating under pressure-driven flow. This document is to be divided accordingly. First the design, development, and characterization of the flow device is presented. Followed by a

presentation of the background theory necessary to discuss droplet formation. Experimental observations are presented and discussed. Finally, a conclusion is presented that describes the major accomplishments and courses of further investigation.

# Chapter 2

## System Development

### 2.1 Design

System design is covered here with the intent of allowing for future modification or reproduction of the flow system. Development of neither the labVIEW Virtual Interface (VI) nor microcontroller code are covered in detail but are presented in the attached appendixes. The technical skills required to build the system include analogue and digital electronics but are of basic undergraduate level and are not covered in any detail here.

**Design Inputs** High level design inputs were generated and may be summarized as follows:

1. The flow system shall be controlled by a labVIEW VI.
2. The flow system shall feature four discrete pressure channels.
3. The flow system shall be capable of producing pressure output from 0 to 1 bar.
4. The resulting controlled pressure shall be visible to and recordable by the user.

**System Components** In order to develop a system capable of meeting these design inputs several key components are required, specified in Table 2.1

Component	Manufacturer	Part Number	Quantity
Regulators	Marsh Bellofram	Type 2000	4
0-1000mbar Transducer	AMS	5915-1000-D	4
0-350mbar Transducer	AMS	5915-0350-D	4
DACs	MCP	4921	4
Microcontroller	Arduino	Uno R3	1

Table 2.1: Key System Components

Alternative components may be acceptable, even superior, to those detailed here. Specifically, pressure transducers that allow for faster modulation may be sought. The time response of the system developed here is covered in Section 2.2. In addition to the key components listed here other basic electrical components were required including standard off-the-shelf resistors, capacitors, molex-connectors and prototyping solderboard.

The system electronics are packaged within a IP 66/IP 67 DIN EN 60529 rated enclosure, shown in Figure 2.1 on the next page. The system functions as a 'black box' with the 240VAC→9VDC power input, USB communication, main pneumatic supply line input, and 4 discrete regulated pressure outputs.

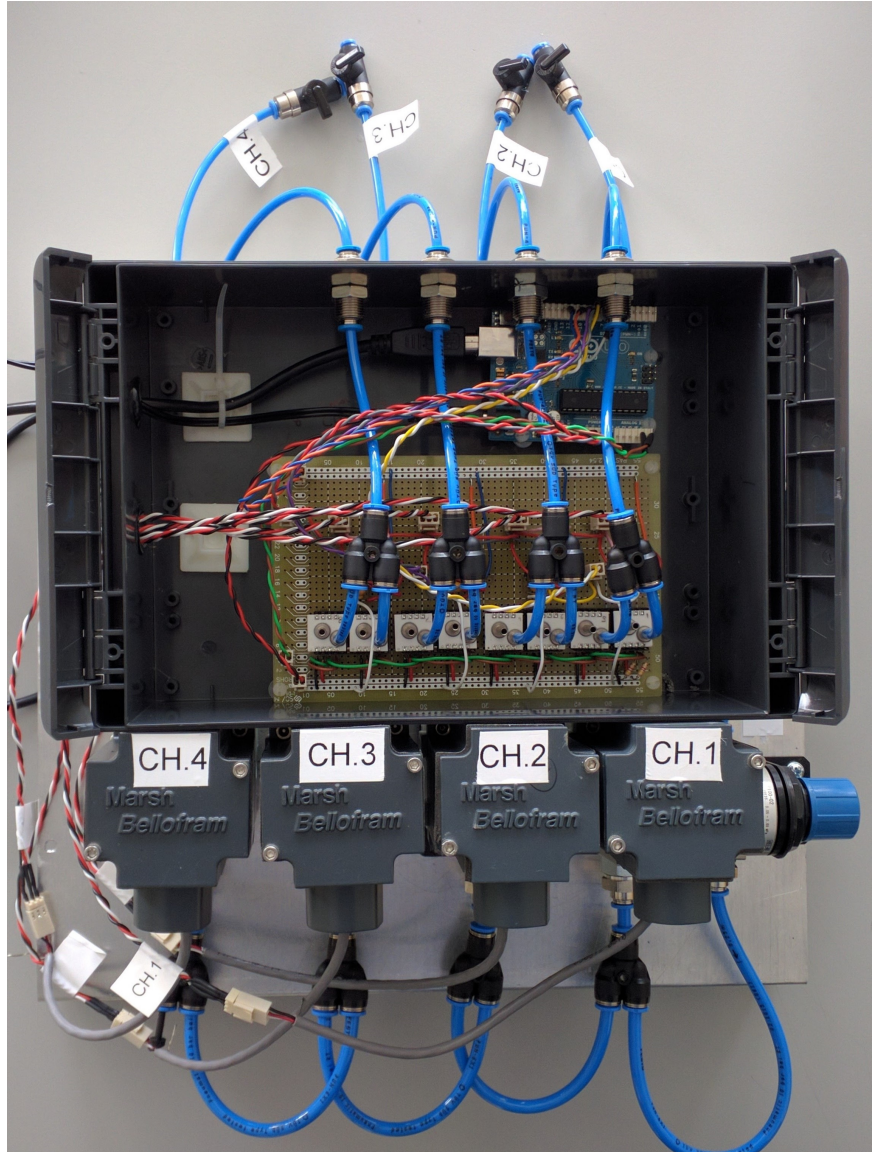


Figure 2.1: The PDFC as contained in the final enclosure.

Several pneumatic components are required to provide a compressed gas flow path between the supply, regulators, transducers, and reagent reservoirs. These components are summarized in the pneumatic schematic for a single channel as shown in Figure 2.2 on the following page. Note that the air supply here is expected to be filtered to remove excess humidity and provide 3 micron particle filtration.

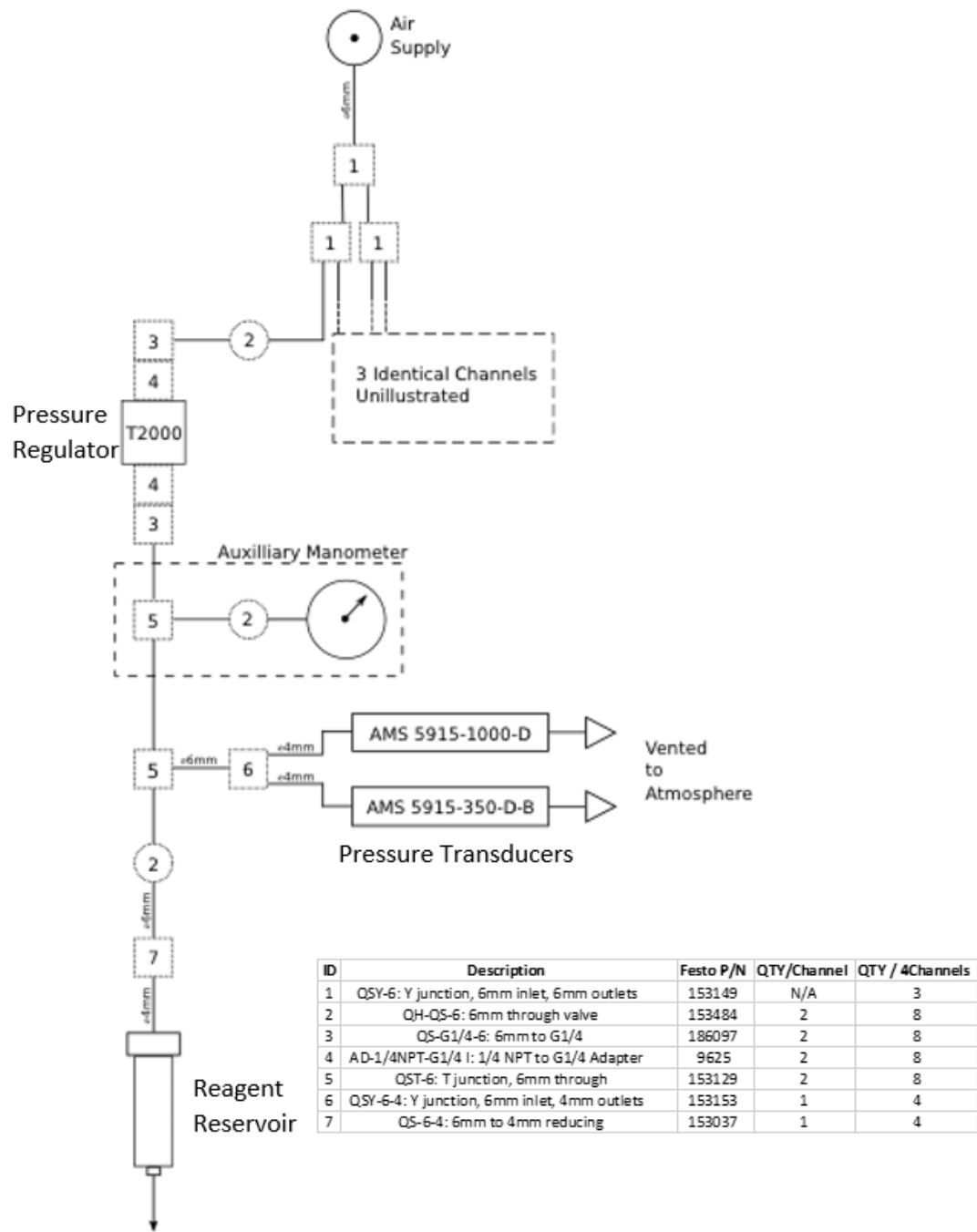


Figure 2.2: The pneumatic schematic detailing a single channel of the PDFC. The four primary components moving down through the schematic are the supply, T2000 pressure regulator, AMS pressure transducers, and the terminal reagent reservoir.

**Operational Overview** The PDFC system is designed to be managed by interaction with a custom LabVIEW VI. The user manually enters a desired control signal within the labVIEW interface of 0 to 5 volts, corresponding to operational pressure range of 0 to 1000mbar.

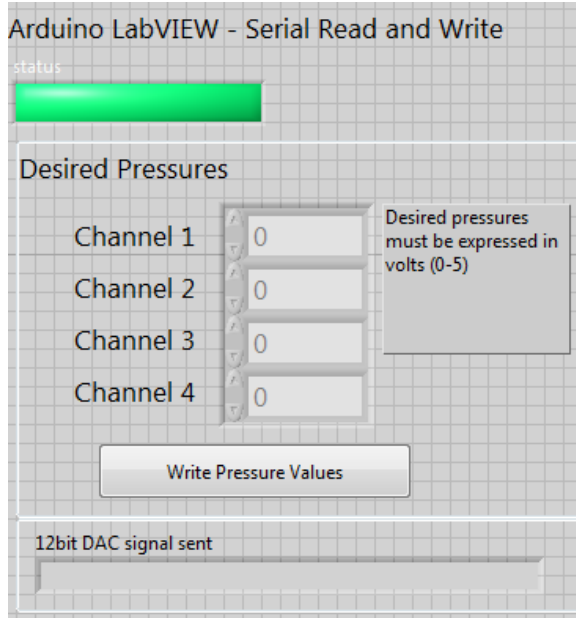


Figure 2.3: Control pressures are set digitally within the LabVIEW interface.

After initiating the write command the digital signal is written synchronously to the microcontroller by Universal Serial Bus (USB) via LabVIEW's 'virtual instrument software architecture' (VISA). The signal is initially sent and interpreted as a string and is processed via the embedded microcontroller code into a binary command comprised of the 4 configuration bits and 12 data bits. This binary command is then written to the digital analogue converters (DACs) via standard serial peripheral interface (SPI) protocol. The DACs convert the binary commands into analogue voltage outputs of 0-5V. This voltage is routed to the input of each pressure regulator and results in the desired pressure output of 0 to 1000 mbar.

The controlled output of each pressure regulator is then split by a y-connector. One flow path goes to the reagent reservoir to drive fluid flow, the other is routed back into the PDFC for real-time measurement by the integrated circuit pressure transducers. Each regulated pressure channel is measured by two different 14bit transducers, one is low range (0-350mbar) with increased resolution, the other is full range (0-1000mbar). The pressure transducers produce a digital signal that is then transferred back to the micro-controller via Inter-Integrated Circuit ( $I^2C$ ) protocol.

Finally, the measured pressures are sent to the LabVIEW VI for display and optional recording. This entire control process including LabVIEW and microfluidic device integration is summarized in system overview shown in Figure 2.4.

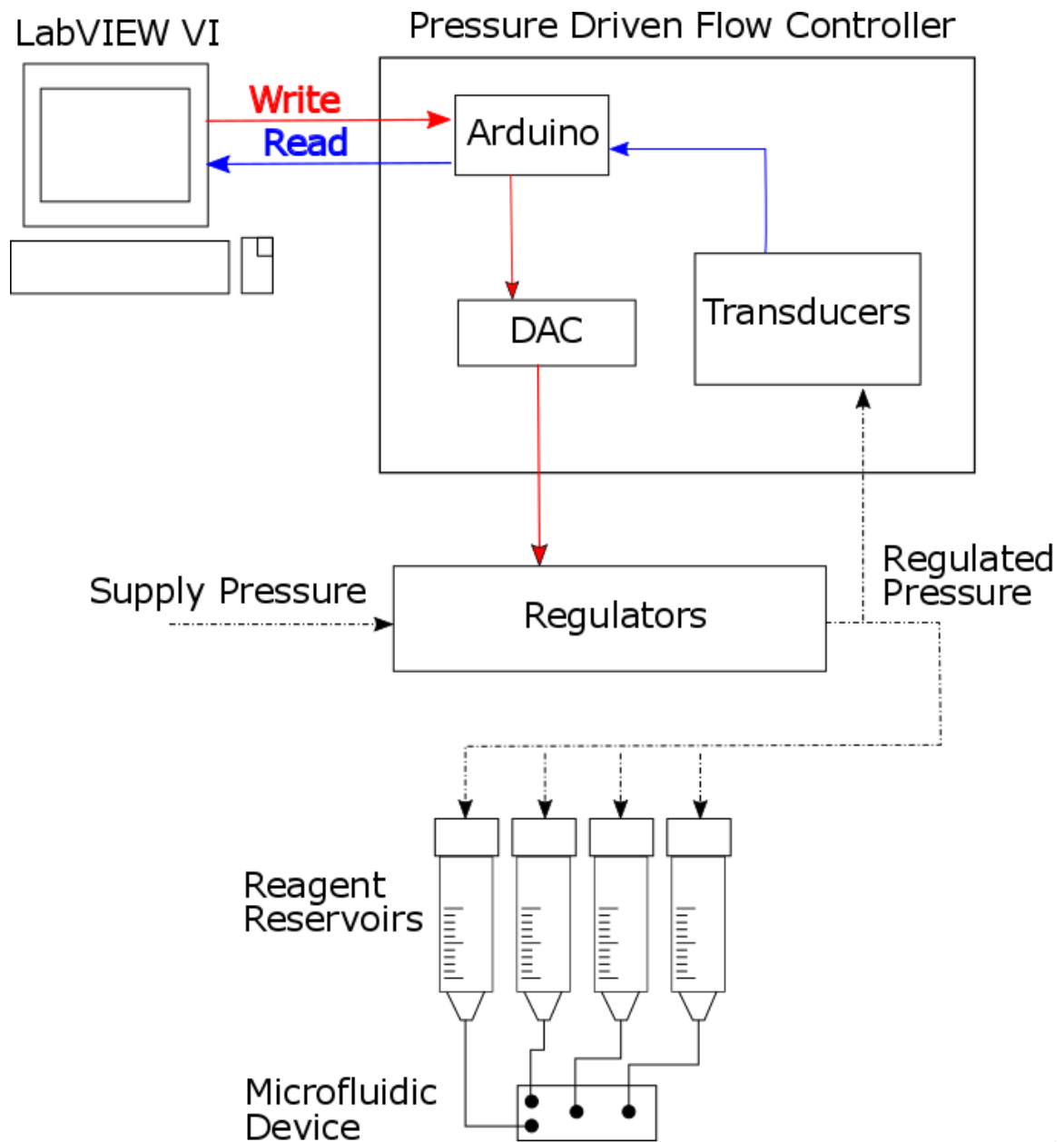


Figure 2.4: System overview showing the control loop used to write (red) and read (blue) channel pressures using the PDFC

## 2.2 Characterization

After completing the design and manufacturing of the PDFC it must be validated prior to being used as a research tool. Particular emphasis is placed on two operating criteria of the system:

1. The response time of the system, from application of write signal to regulated pressure response.
2. The accuracy and channel-to-channel variance observed in the system.

In regards to the response time of the system it may be valuable to detail the magnitude of individual response times for the process steps required from signal input to response output, summarized in Table 2.2. The relative time response of each process step was determined either by manufacturer data sheets or experimentally, as shown in Figure 2.5 on the next page.

Process Step	Magnitude of Time Response(ms)
Sync. USB Comm.	1000
Arduino String – > Binary	1
DAC	0.01
Pressure Regulator	100

Table 2.2: Component Response Time

The labVIEW VI is capable of recording the measured regulated pressure outputs, which may be used to document control pressures utilized for specific experimentation. Here, that data logging capability is used to investigate the system's time response, as shown in Figure 2.5 on the following page. The gap in data is due to use of 'synchronous' USB communication within the LabVIEW environment, which prevents simultaneous read/write capabilities. The leftmost data prior to the gap coincides with the time point at which the command signal is sent. While all channel outputs clearly converge to the desired nominal output pressure, variation in channel regulation is apparent as the pressure output stabilizes. Variation in the stabilization of regulated signal is due to differences in the control circuit from regulator to regulator. The model of regulator used here relies on a Proportional Integral Differential (PID) control circuit with manually adjustable potentiometers to adjust gain constants, non-ideal when attempting to produce coincident outputs on discrete channels.

The time from signal write to that of reaching 95% of the desired output increases as a function of differential pressure sought but is roughly on the magnitude of 1sec.

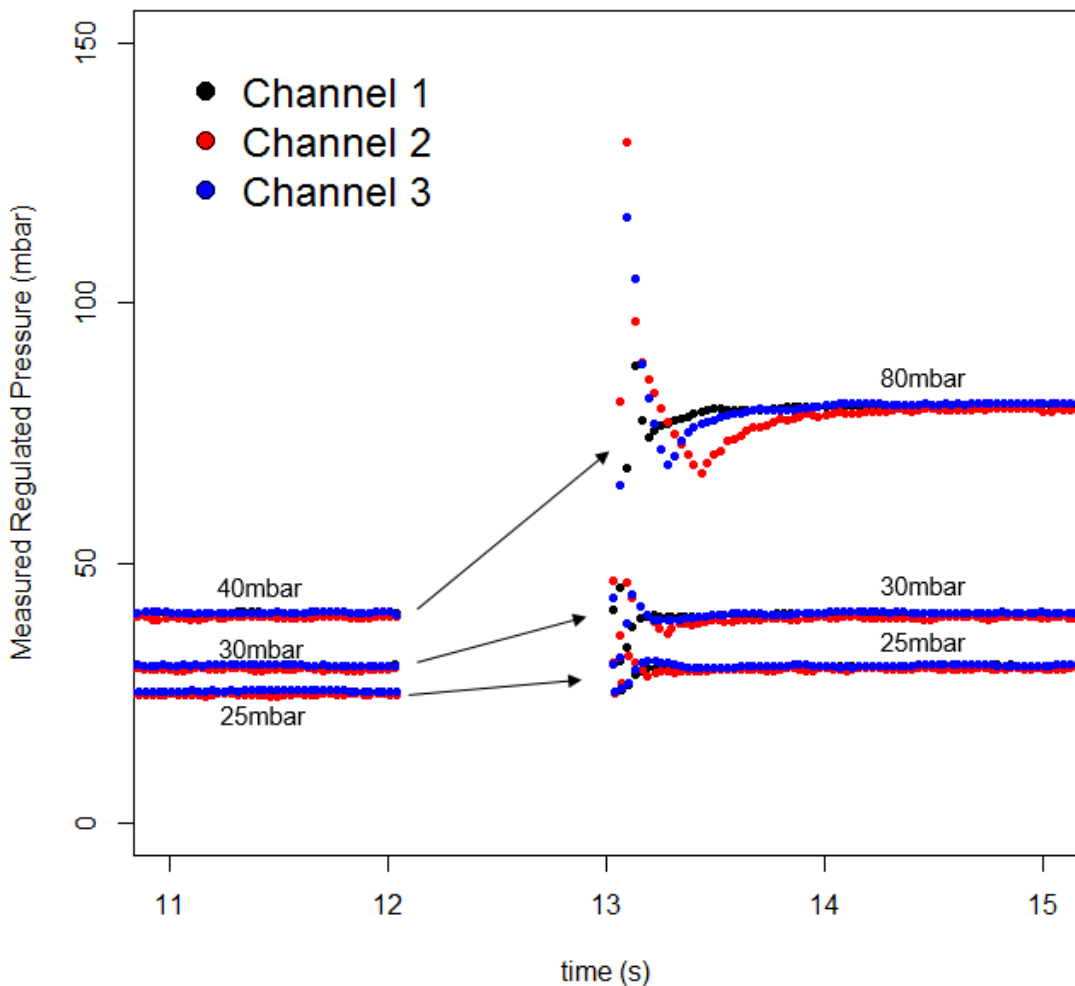


Figure 2.5: Three pressure transitions are shown, 40 to 80mbar, 30 to 40mbar, and 25 to 30mbar for 3 discrete output channels.

These observations suggests that the system, as currently developed, is not appropriate for the millisecond or faster response times required for real-time manipulation of droplet size. This agrees with previous findings. Flowrate control of droplet formation is known for its slow response whether by syringe pump or pressure flow. Furthermore, response time of the actual device is further delayed due to fluidic capacitance caused by the compressibility of reagents, tubing and PDMS channels [9, 20]. If fast-response times are sought a more appropriate methodology may be to maintain a steady flowrate and drive droplet formation by active methods through di-

rect manipulation of the fluid at the local point of formation by electrical, mechanical, magnetic, or acoustic means [7].

System accuracy and channel-to-channel variation can be investigated in a similar method to time response. Here, three channels are simultaneously regulated to a nominal 100 mbar. After a stabilization time of approximately 3 seconds, a 15 second mean and standard deviation are acquired for each channel, as shown in area between the dashed lines in Figure 2.6. Each channel is capable of regulating to the nominal  $100 \pm 1$  mbar with a standard deviation of less than 0.25 mbar. The capability to maintain stable pressure and hence steady flow is critical for production of highly monodispersed droplets, as documented in Results section 4.3.

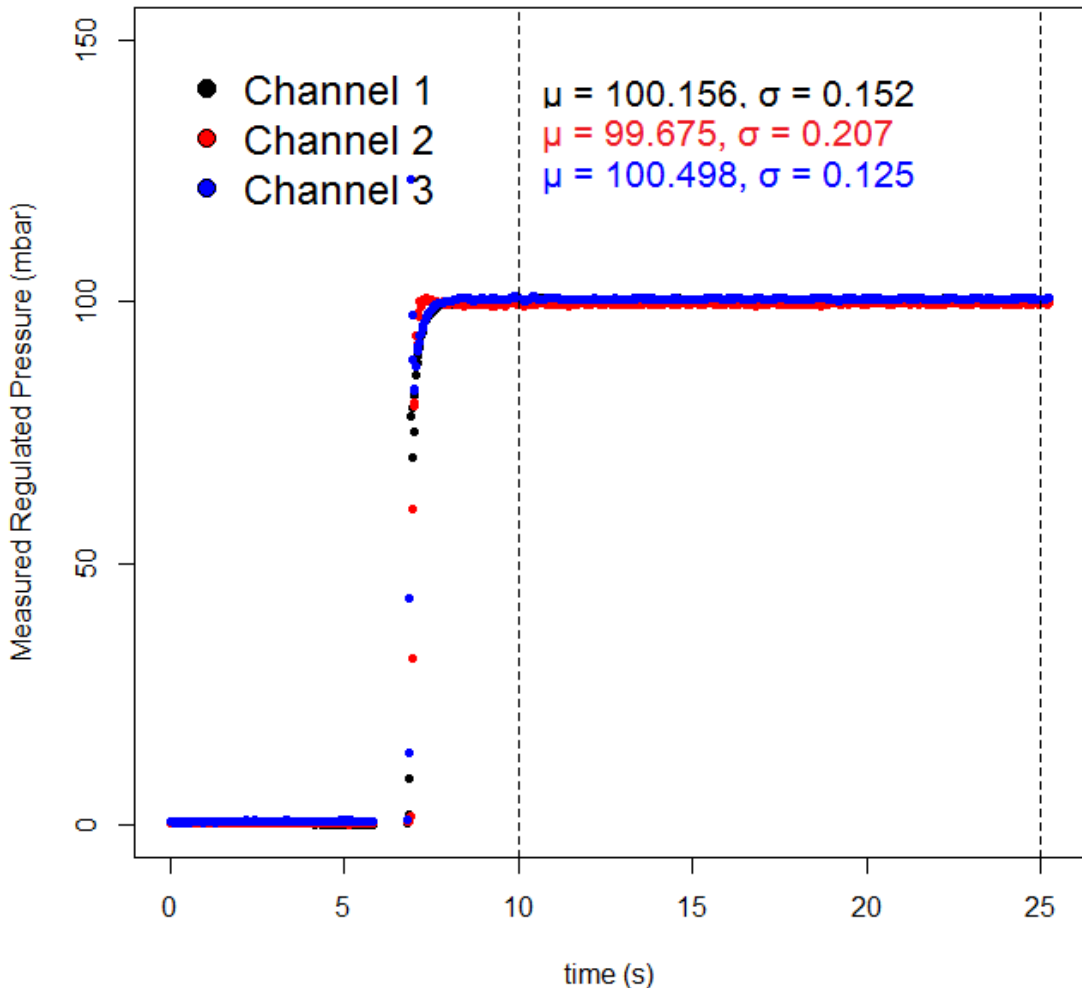


Figure 2.6: Accuracy and channel-to-channel variation of the PDFC system.

# Chapter 3

## Background Theory

### 3.1 Fluid Dynamics at the Microscale

Development of a pneumatic pressure driven flow system for use in microfluidic research requires a firm grasp on the transition from 'macro' fluidics to microfluidics. The system operates across a great range of scales, drawing and compressing air from a room of several cubic meters that is subsequently used to provide flow in micrometer-wide channels. Following the flow path of the system - compressed air is filtered and directed via large diameter ( $\approx 5\text{mm}$ ) tubing to reagent columns of large diameter ( $\approx 2\text{cm}$ ), where the compressed air acts on the reagent to produce flow through smaller tubing ( $\approx 0.5\text{mm}$ ) before finally transitioning into the microfluidic device channels ( $\approx 30\mu\text{m}$ ).

The study of fluid dynamics requires the analysis of individual fluid forces, such as gravitational, inertial, viscous, and interfacial forces [5]. An understanding of how these force groups combine is required to define flow behavior. In order to understand the transition from large dimension to small dimension systems it may be useful to understand how these forces relate to system dimensions by the way of scaling laws. Some fluid forces such as inertial forces and gravitational forces are dependent on the *volume* of fluid involved. Other fluid forces are intrinsically defined by the *surface area* of the fluids such as viscous and interfacial forces. More broadly speaking each of the various fluid forces may be dependent on different orders of characteristic length,  $l$ . For example, inertial force is dependent on density,  $\rho$ , which may be expressed as mass per volume, or mass per  $l^3$ , as shown in Equation 3.1 on the following page. Similarly, interfacial tension is often defined as the partial differential of the Gibb's free energy over area, where the area term may be expressed in terms of  $l^2$ , shown in Equation 3.2 on the next page [3].

$$i = \rho\nu^2 = \frac{m}{V}\nu^2 = \frac{m}{(l^3)}\nu^2 \quad (3.1)$$

$$\gamma = \frac{\partial G}{\partial A} = \frac{\partial G}{\partial(l^2)} \quad (3.2)$$

Consider the relative effect these individual forces have on the overall fluid behavior in which the volume dependent forces have an  $l^3$  term and the surface forces have a  $l^2$  term, as shown in Equation 3.3 [5]

$$\frac{\text{Surface Forces}}{\text{Volume Forces}} \propto \frac{l^2}{l^3} = l^{-1} \lim_{l \rightarrow 0} \rightarrow \infty \quad (3.3)$$

From this comes the realization that as systems are miniaturized towards a theoretical zero-dimension the surface forces begin play an exponentially larger effect relative to the volume forces.

## 3.2 Droplet Microfluidics Overview

Droplet microfluidics is a general term used usually to refer to a two component emulsion system. The two liquid components, often referred to as phases, function as a analyte vessel and a vessel carrier. The analyte vessel is typically aqueous and due to the fact that the droplets are discrete the phase is generally referred to as the discontinuous phase. The carrier solution, generally an oil, preferentially wets the device's channel walls and is responsible for carrying the droplets [13]. The carrier phase is herein referred to as the continuous phase.

Formation of droplets using T-junction devices was first described by Thorsen et al in 2001 [22]. The T-junction device functions by introducing the discontinuous phase perpendicularly into the main continuous phase channel. The force dynamics that dictate droplet break-up were first described to be a balance between viscous shear and interfacial forces. Later, Gastecki et al, showed that at low capillary numbers break-up is no longer driven by viscous forces but is due to a pressure differential caused by blocking of the main channel by the discontinuous phase [12]. This realization lead to the declaration of two stable droplet formation regimes, Dripping and Squeezing. The *Dripping Regime* is described by a domination of viscous forces associated with the continuous phase flow which are significantly large to cause shearing of the immiscible thread and the production of a droplet prior to blocking the outlet channel. The *Squeezing Regime* occurs when the discontinuous phase blocks the majority of the outlet channel prior to collapse and droplets are formed by a squeezing effect due

to the pressure build up caused by the blocked channel [18]. The fluid and flow parameters that determine the acting regime include fluid viscosities, flowrates and interfacial tensions. The transition between these regimes has been described both experimentally and in numerical simulations [8, 11].

**Dimensionless Groups** In many cases fluid flow at the microscale can be best categorized by comparing *dimensionless groups* driven by fluid parameters such as viscosity, velocity, density and system geometry, as is the case of the dimensionless group known as Reynold's Number ( $Re$ ) shown in Equation 3.4. The  $Re$  value can be described in real world terms as a relation between the inertial forces and viscosity forces at play in a system.

$$Re = \frac{\rho \nu L}{\mu} \quad (3.4)$$

Where  $\rho$  is fluid density,  $\nu$  is fluid velocity,  $L$  is characteristic length, and  $\mu$  is fluid viscosity. As the majority of microfluidic systems feature small characteristic lengths, inertial forces are overwhelmed by viscous forces resulting in laminar flow and the  $Re$  value becomes less valuable in the differentiation and categorization of different systems [14].

The Capillary number ( $Ca$ ) is a dimensionless group that compares the relative contribution of interfacial forces and viscous forces. The capillary number is especially useful in discussion of two-phase microfluidic systems because it neglects any inertial forces and is capable of describing droplet formation behavior as influenced by solution viscosity and surface energies. The  $Ca$  is defined as shown in Equation 3.5 [6].

$$Ca = \frac{\mu u}{\gamma} \quad (3.5)$$

Where  $\mu$  is defined as the viscosity of the continuous phase,  $u$  is the mean continuous phase velocity, and  $\gamma$  is the interfacial tension between the discontinuous and continuous phases. The viscous forces and interfacial forces determining fluid behavior are generally understood to act tangentially and normal to the two-phase interface, respectively. Viscous forces along the droplet surface work in elongation of the surface of the droplet whereas interfacial forces work to minimize the interfacial area. These two opposing behaviors when acting in different ratios dictate the droplet behavior as categorized by the different fluid regimes squeezing, dripping, and jetting [19].

### 3.3 Determining System Flowrates

One of the challenges in using pressure-driven flows for microfluidic research is the difficulty in determining local fluid velocities and flowrates within the microfluidic device. Several approaches are available to approximate the local device flow rates:

1. Experimentally: once the system is primed and running, the waste reservoir can be weighed over some time interval,  $t$ , to determine the accumulation of fluid mass,  $M$ . Assuming the density of reagents is known,  $\rho$ , the mean flowrate,  $Q(m^3 s^{-1})$ , can be calculated as  $Q = \frac{M}{\rho t}$ .
2. Experimentally: while running, a visual indicator (such as beads, or droplets) can be measured by high speed camera to obtain an object velocity,  $V$ . Assuming the cross-section of the channel is known,  $A$ , the flowrate can be calculated as  $Q = V \times A$ .
3. Numerical Approximation: Assuming that all system dimensions and applied pressures are known, flowrates can be approximated by the analogous use of Ohm's Law,  $\Delta V = IR$ . Where voltage,  $V$ , current,  $I$ , and electrical resistance,  $R$ , are analogous to pressure, flow, and hydraulic resistance, respectively.

Here, the velocity and flowrate of the continuous phase are determined by the second method, experimentally measuring the velocity of the produced droplets. This method is limiting in that the continuous phase velocity is a relatively complex Poiseuille flow field [5], and measuring the droplet velocity is only an approximation. Furthermore, the method does not allow measurement of the discontinuous phase flowrate. In order to better understand these intricacies it may be valuable to evaluate the system's hydraulic resistance.

**Hydraulic Resistance** In order to numerically approximate the flowrate of microfluidic systems by use of hydraulic resistance a fundamental understanding of the Hagen-Poiseuille law is required. As previously stated, pressure, flowrate, and hydraulic resistance are analogous to Ohm's law as shown in Equation 3.6 [5].

$$\Delta p = R_{hyd}Q \quad (3.6)$$

The SI units of Hagan-Poiseuille are as shown in 3.7.

$$[Q] = \frac{m^3}{s} \quad [\Delta P] = Pa = \frac{kg}{ms^2} \quad [R_{hyd}] = \frac{kg}{m^4 s} \quad (3.7)$$

The hydraulic resistance varies based on specific channel geometry but the presence of a characteristic length to the fourth power is universal, shown in Equation 3.7. This suggests that as channel dimensions increase the resistance decreases in a manner proportional to the dimensional change to the fourth power. This proportionality can be used to simplify the overall system considerably. Consider the simple generic system as shown in Figure 3.1.

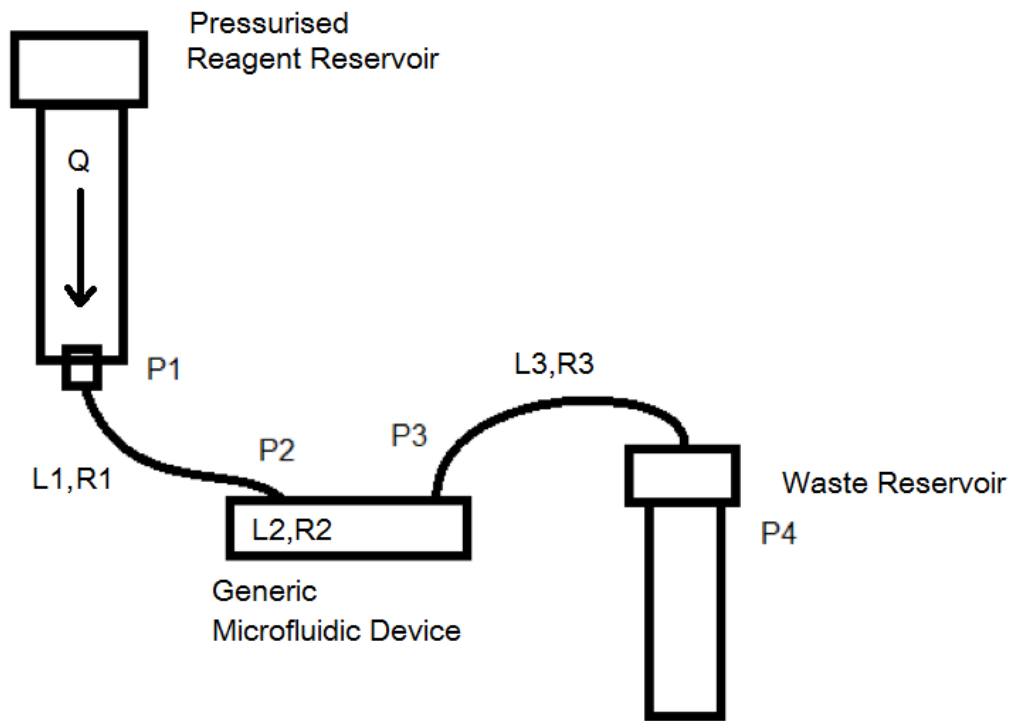


Figure 3.1: The microfluidic system detailed from the reagent water column to the waste reservoir.

The fluidic resistance due to the reagent reservoirs and tubing leading to the microfluidic device contribute to overall system resistance, and therefore flowrate. However, if the reservoir and tubing widths are substantially larger than the microfluidic device's channels the resistance and therefore contribution to system's pressure loss may be neglected.

For the purpose of quantifying the contribution to total pressure loss of tubing in a generic system the following arbitrary values are applied: Assume that  $P_4$  is equivalent to atmospheric pressure, 0 Pa, and  $L_1 = L_3 = 0.500 \text{ m}$ ,  $L_2 = 0.010 \text{ m}$ , viscosity  $n = 1 \text{ cP} = 0.001 \text{ Pa s}$ , tube radius  $r = 0.00025 \text{ m}$  and channel height

$h = 0.00005m$ . Take  $P_1 = 500 \text{ mbar} = 50 \text{ kPa}$  which is mid operational range for the system.

Consider the simple case shown in Figure 3.1 on the preceding page, and that hydraulic resistances in straight circular and square channels can be approximated as shown in Equations 3.8 and 3.9, respectively [5].

$$R_1 = R_3 = \frac{8\eta L}{\pi r^4} = \frac{8(0.001)(0.500)}{\pi 0.00025^4} = 3.26 \times 10^7 \frac{\text{kg}}{\text{m}^4 \text{s}} \quad (3.8)$$

$$R_2 = \frac{28.4\eta L}{h^4} = \frac{28.4(0.001)(0.010)}{0.00005^4} = 4.54 \times 10^{13} \frac{\text{kg}}{\text{m}^4 \text{s}} \quad (3.9)$$

Clearly the resistance seen over the length of the simplified microfluidic device of cross-section  $50\mu\text{m} \times 50\mu\text{m}$  is several orders of magnitude greater than the resistance of the system's input and output tubing. The flowrate can be calculated as shown in 3.10.

$$P_4 - P_1 = (R_1 + R_2 + R_3)Q$$

$$Q = \frac{P_4 - P_1}{(R_1 + R_2 + R_3)}$$

$$Q = \frac{50,000}{(2(3.26 * 10^7) + 4.54 * 10^{13})} = 1.10 \times 10^{-9} \frac{\text{m}^3}{\text{s}} = 1.10 \times 10^{-6} \frac{\text{L}}{\text{s}} \quad (3.10)$$

Assuming that the system is at steady state and therefore the microfluidic structure (tubing and PDMS) is not expanding due to internal pressure we can infer by conservation of mass and incompressible fluids that the volumetric flowrate is constant across each of the system pressure points shown in Figure 3.1 on the preceding page. Taking this constant flowrate and the previously calculated, resistances individual pressure drops can be calculated as shown in Equation 3.11.

$$\begin{aligned} P_2 - P_1 &= (R_1)Q = 3.59 \times 10^{-2} \text{ Pa} \\ P_3 - P_2 &= (R_2)Q = 4.99 \times 10^4 \text{ Pa} \\ P_4 - P_3 &= (R_3)Q = 3.59 \times 10^{-2} \text{ Pa} \end{aligned} \quad (3.11)$$

In this simplified case, representative of a typical microfluidic experimental set-up, the pressure loss due to the tubing relative to the total pressure drop can be calculated as shown in Equation 3.12

$$\frac{(P_2 - P_1) + (P_4 - P_3)}{P_4 - P_1} = \frac{3.59 \times 10^{-2}}{50.00 \times 10^3} = 7.18 \times 10^{-7} \quad (3.12)$$

As the contribution to pressure loss is so small ( $<< 1\%$ ), it may be appropriate to neglect the tubing and assume that the PDFC applied pressure is equivalent to the pressure applied across the microfluidic device. This allows the device's pressures to be simplified as shown in Figure 3.2. The local pressures at the T-junction can then be estimated using the Hagan-Poiseuille law if the channel resistance and flowrates are known.

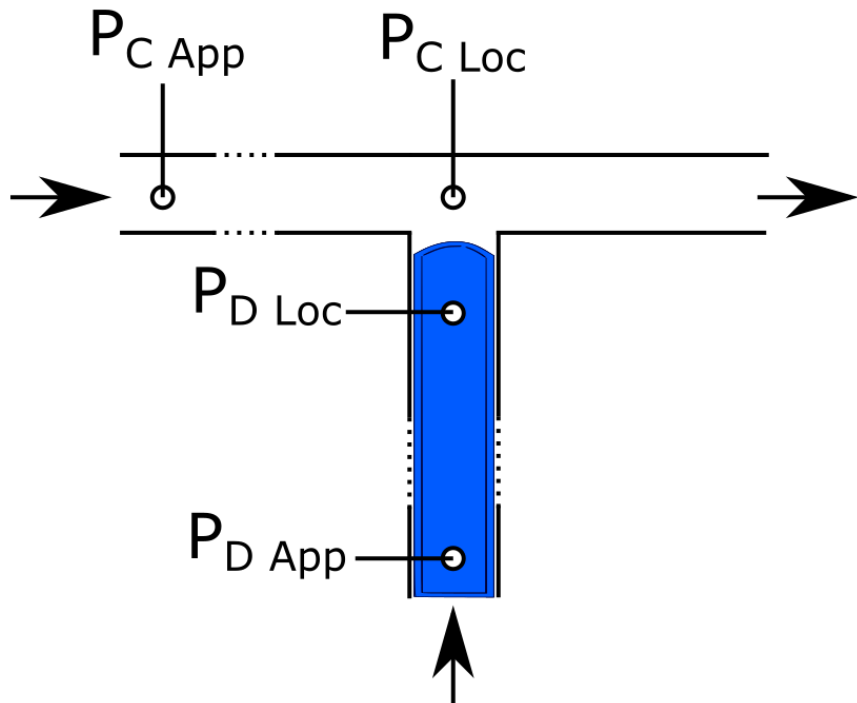


Figure 3.2: Pressure balance at no-flow condition, where  $P_{C App}$  and  $P_{D App}$  are the pressures applied to the continuous and discontinuous phases and  $P_{C Loc}$  and  $P_{D Loc}$  are the local pressures at the T-junction. The dashed lines represent the channel geometry present between the device inlets and the T-junction.

One further point, highlighting the difference between volumetric and pressure-driven flows, is the existence of a quasi-equilibrium no flow condition. As the system is moved towards the lowest operational pressure ratios, the aqueous phase comes to a quasi equilibrium no-flow state, as previously reported by Ward *et al.* [23]. If the pressure ratio is decreased any further(either by increasing  $P_{Oil}$  or decreasing  $P_{H_2O}$ ) back-flow will occur, in which the continuous phase begins displacing the aqueous phase upstream towards the reservoir. This quasi equilibrium state may be described as a balance of forces between the pressure of the two phases and the Laplace pressure differential across the liquid-liquid interface, described as shown in Equation 3.13 on the following page.

$$P_{D_{Loc}} + P_{Laplace} = P_{C_{Loc}} \quad (3.13)$$

Where Laplace pressure can be roughly approximated given  $\gamma$  is the interfacial tension between the two phases,  $r$  is the radius of curvature of the interface as shown in Equation 3.14 [5]:

$$P_{Laplace} = \frac{2\gamma}{r} \quad (3.14)$$

It should be noted that here  $P_{D_{Loc}}$  and  $P_{C_{Loc}}$  represent the pressures of the two phases local to the T junction and that there is some unknown pressure drop between the applied control pressures at the inlet reservoirs and these local pressures.

# Chapter 4

## System Application - Droplet Microluidics

### 4.1 Aims

The application of the PDFC to droplet microfluidics serves two purposes. First, it verifies that the system is functioning as intended for use as a practical research tool. Second, it allows the characterization of droplet formation by a pressure driven flow in T-junction geometry, an area currently underdeveloped [8].

### 4.2 Methods

#### 4.2.1 Device Generation

The T-junction microfluidic device referenced herein is fabricated using standard soft lithography methods [21]. Two part Polydimethylsiloxane (PDMS) was poured onto a SU-8 mold previously developed by Schmid and Franke [17] to form an array of individual  $25\mu m \times 25\mu m$  T-junction channels. The PDMS was cured at 65dC for 3 hours. After cooling to room temperature, the set PDMS was cut and removed from the mold. Tubing connection holes were punched using a standard 0.5mm biopsy punch. Next, a standard glass slide and the PDMS channels are oxygen-plasma treated, adhered, and exposed to 100dC for 1hour. Prior to use, devices are treated with the aquapel for 10mins, purged with filtered compressed gas and dried at 65dC for 3 hours.

### **4.2.2 Reagents**

Reagents were formulated in bulk, the same formulation was used for all data presented here. The continuous phase consists of 3M’s HFE-7500 fluorocarbon oil stabilized with fluorosurfactant ammonium carboxylate DuPont Krytox 157 to concentration of 2.0 wt%. This discontinuous phase consists of de-ionized water and Sigma Aldrich’s B0126-256 Bromophenol blue, dissolved in 0.1M NaOH, to a final concentration of 1mM.

### **4.2.3 Experimental Procedure**

The microfluidic device was installed on an upright microscope with 20X Objective and brightfield illumination. Images are acquired by Photon fastcam at 500 frames per second (fps). The devices were first primed with the oil phase to preferentially wet the channel walls prior to introduction of the aqueous phase. The applied control pressure was held constant for the continuous phase while varying the discontinuous phase control pressure to achieve varying flow conditions. Discontinuous phase control pressure was varied at intervals no smaller than  $\approx$ 5mbar until droplet formation ceased due to the onset of backflow or instability, for low or high pressures, respectively.

### **4.2.4 Analysis of Collected Data**

The captured images were then analyzed using a custom imageJ script, shown in Figure 4.1 on the following page. The script differentiates the droplets from the carrier fluid to determine droplet length,  $L$ , position,  $X$ , along an arbitrarily defined axis parallel to the geometry’s outlet channel and the frame at which the measurement occurs.

```

V2B_script_T-junction2.ijm
File Edit Font Examples Macros Debug
// Increase the contrast to improve differentiation between droplets and carrier fluid
run("Enhance Contrast", "saturated=0.35");

//Convert to binary image using constant threshold values
setThreshold(8,32);
run("Convert to Mask", "method=Huang background=Light");
makeRectangle(300, 18, 450, 48);
run("Crop");
run("Fill Holes", "stack");

//Crop image to include only the droplets
makeRectangle(0, 5, 450, 35);
run("Crop");

//Canvas size must be increased vertically, so that the exclude edges function can be used
run("Canvas Size...", "width=500 height=60 position=Center zero");

//Analyze particles
run("Analyze Particles...", "size=100-Infinity exclude clear add stack");
//Measure using roiManager
run("Set Measurements...", "area bounding stack redirect=None decimal=3");
roiManager("Measure");

//save data automatically
dir = "C:\\Users\\Aaron Delahanty\\Desktop\\DDMM\\YYYY\\";
name = getTitle;
path = dir+name;
saveAs("text",path);

close();

```

Figure 4.1: Custom imageJ script used to isolate and measure droplets.

## 4.3 Results

### 4.3.1 Regime Transition

For the T-junction channel geometry described, the dimensionless droplet ratio of droplet length,  $L$ , over channel width,  $W$ , is plotted as a function of the applied control pressure ratios,  $\frac{P_{H_2O}}{P_{Oil}}$ , shown in Figure 4.2 on the next page. Error bars have been calculated by standard deviation of measured droplet length which results in error equal to or smaller than the symbol size and thus not shown. Linear regression models have been applied to the data points expected to be within the squeezing regime. The slopes of the fitted lines were determined as 3.909, 4.151, and 5.370

for applied continuous phase pressures of 40, 60, and 80 mbar with coefficients of determination of 0.958, 0.996, and 0.990, respectively. Full summary statistics of the linear regression fit are presented in the Supplementary Statistics Appendix.

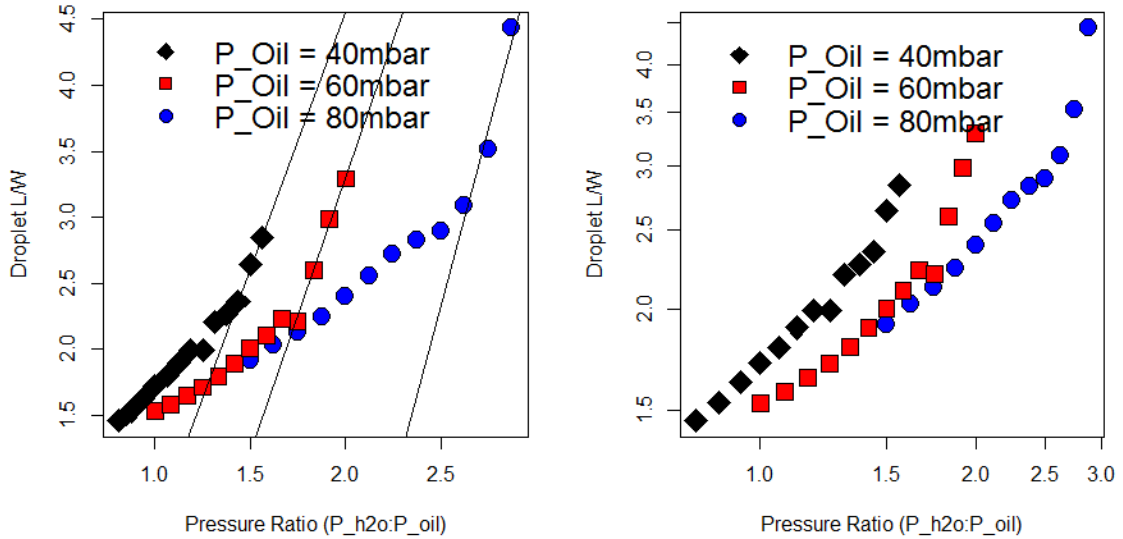


Figure 4.2: Standard (left) and log-log (right) plots of droplet length as a function of the applied control pressure ratio for T-junction geometry. Note the distinct change in slope as the pressure ratio increases, an indication of regime transition.

Outer Ca values are calculated given an interfacial tension of  $\gamma = 2.87 \times 10^{-3} \frac{N}{m}$  (as measured by spinning method), continuous phase viscosity of  $\mu = 1.24 \times 10^{-3} Pa \cdot s$ [1], and mean velocity,  $u$ , as determined by droplet position over consecutive frames.

Droplet length is plotted as a function of capillary number as shown in Figure 4.3 on the following page for each of the applied continuous pressures. The critical capillary numbers were approximated as 0.0135, 0.0185, and 0.0215 for 40, 60 and 80 mbar continuous phase pressures, respectively. Images of droplet formation are shown within the squeezing and dripping regimes for each continuous phase control pressure. The images shown are captured one frame prior to droplet formation.

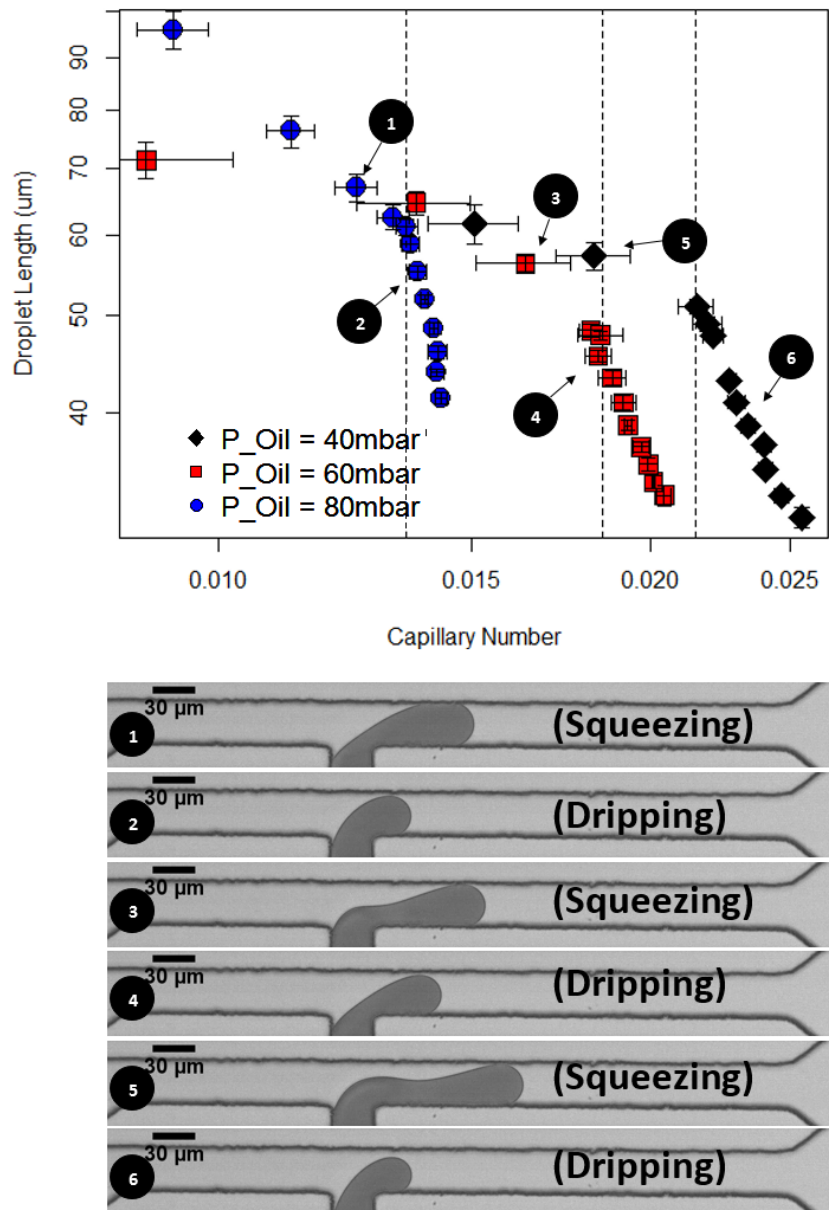


Figure 4.3: Top: Droplet length as a function of Capillary number across squeezing and dripping regimes. The transition between dripping and squeezing regimes is marked by vertical dashed lines, corresponding to critical capillary numbers of 0.0135, 0.0185, and 0.0215. Bottom: Typical images of droplet elongation just prior to formation.

### 4.3.2 Droplet Polydispersity

Variance in droplet dimensions is analyzed by evaluating the length of droplets formed by constant applied control pressures. Images were acquired at 500 fps for a period of 10 seconds resulting in a sample size of at least 100 droplets with at least three length measurements taken in subsequent frames per unique droplet. A variety of plots investigating population statistics are shown in Figure 4.4, for data acquired at  $P_{OIL} = 20\text{mbar}$ ,  $P_{H_2O} = 80\text{mbar}$ , resulting in a  $Ca$  value of 0.010. The same analysis was conducted at two higher  $Ca$  values and is found in the Supplementary Statistics Appendix .

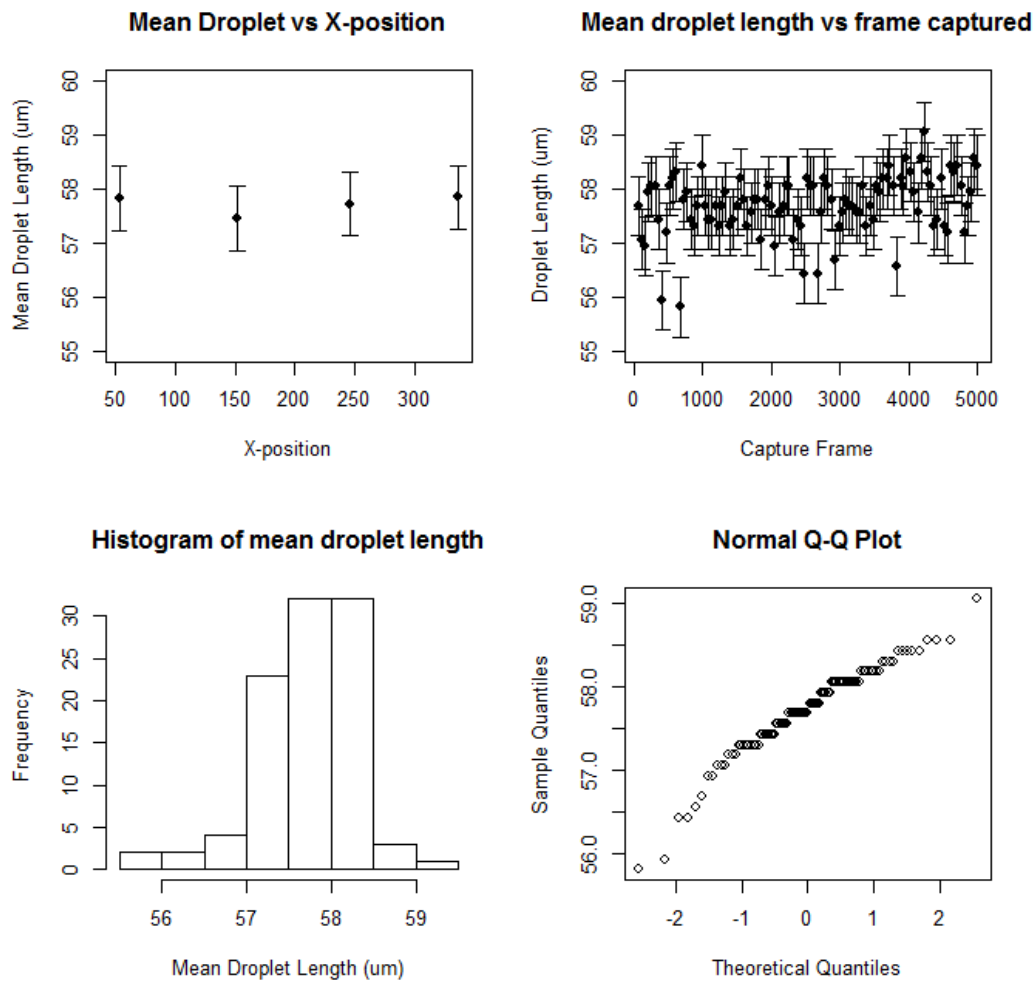


Figure 4.4: Population distribution of droplet length for  $P_{oil} = 0.1\text{bar}$ ,  $Ca = 0.010$ . Top-left: Mean droplet length as shown by measured X-position. Top-right: Droplet length shown over the duration of image acquisition. Bottom-left: Histogram of measured droplet length. Bottom-right: Q-Q plot for the droplet length population.

From the analyzed data, droplet velocity, flowrate, capillary number, mean length, length standard deviation and percent Coefficient of Variation are extracted. A summary of the resulting dimensional statistics is shown in Table 4.1.

$P_{Ratio}$	$V_C(m/s)$	$Q_C(\mu L/min)$	Ca	$MeanLength(\mu m)$	$StdDev(\mu m)$	C.V.
4	0.023	0.863	0.010	57.71	0.55	0.95
2.25	0.033	1.238	0.014	54.53	0.35	0.64
1.66	0.043	1.613	0.018	48.14	0.21	0.43

Table 4.1: Dimensional analysis of droplets

## 4.4 Discussion

### 4.4.1 Droplet Regime Transition

Previous work has been done to establish specific flow regimes in which droplets are formed in T-junction geometry by both numeric modeling and experimental investigations [2, 11, 12]. Previous findings suggest that two stable droplet formation regimes exist in T-junction droplet formation, *dripping* and *squeezing*. In a highly cited paper, De Menech et al showed by numerical modeling that the transition between the two distinct droplet regimes may be defined by a Critical Capillary Number,  $Ca_{cr}$ , and that this transition is independent of viscosity ratio and flowrates. This transition has been previously determined both experimentally and in numerical simulations to be  $Ca_{cr} \approx 10^{-2}$  [8, 11, 24]. These values of Capillary Numbers represent a threshold below which the interfacial forces significantly dominate the viscous forces. Thus, in these geometries, the discontinuous phase is only minimally elongated as it enters the T-junction and instead extends orthogonally to the main channels such that the channel is plugged prior to droplet formation. After the droplet blocks the channel outlet, break-up proceeds driven by the building pressure differential due to the blockage.

*While the regime transition has been well documented through numerical simulations and in experiments utilizing volumetric-flow, to the best of the author's knowledge there has been no record of experimental observations demonstrating the regime transition from squeezing to dripping in a pressure-driven flow system.* This, despite the fact that there have been documented dissimilarities in volumetric versus pressure-driven flow in droplet formation[23], and that there may be advantages in droplet monodispersity in pressure-driven systems [8, 15].

The data presented here shows a distinct transition between dripping and squeezing regimes, as demonstrated by the change in slope shown in Figure 4.2 on page 23. The plot shows a transition from dripping regime to squeezing regime as the pressure ratio increases. The squeezing regime appears to be linear as determined by the linear regression models. This linearity agrees with Gastecki's findings that within the squeezing regime droplet L/W is a function of only the channel geometry, represented by the  $\alpha$  coefficient, and the volumetric flowrates,  $Q_{in}$  and  $Q_{out}$  shown in Equation 4.1 [12].

$$L/W = 1 + \alpha Q_{in}/Q_{out} \quad (4.1)$$

Here, L/W data is presented as a function of applied pressure ratios rather than flowrate ratios and therefore cannot be directly compared. Furthermore, the data

presented here exists precisely at the transitional capillary numbers and therefore contains droplets formed within both regimes as opposed to Garstecki's purely squeezing regime data. Therefore, in order to draw further conclusions regarding droplet dimensions as they pertain to flow ratios in a pressure-driven system both these complications must be overcome.

The transition between regimes may also be shown by the changing behavior of droplet length as a function of capillary number shown in Figure 4.3 on page 24. However, the critical capillary number at which the transition occurs is not universal between the varying flowrates as shown previously [11]. The transitional capillary number can be plotted as a function of the continuous phase pressure as shown in Figure 4.5.

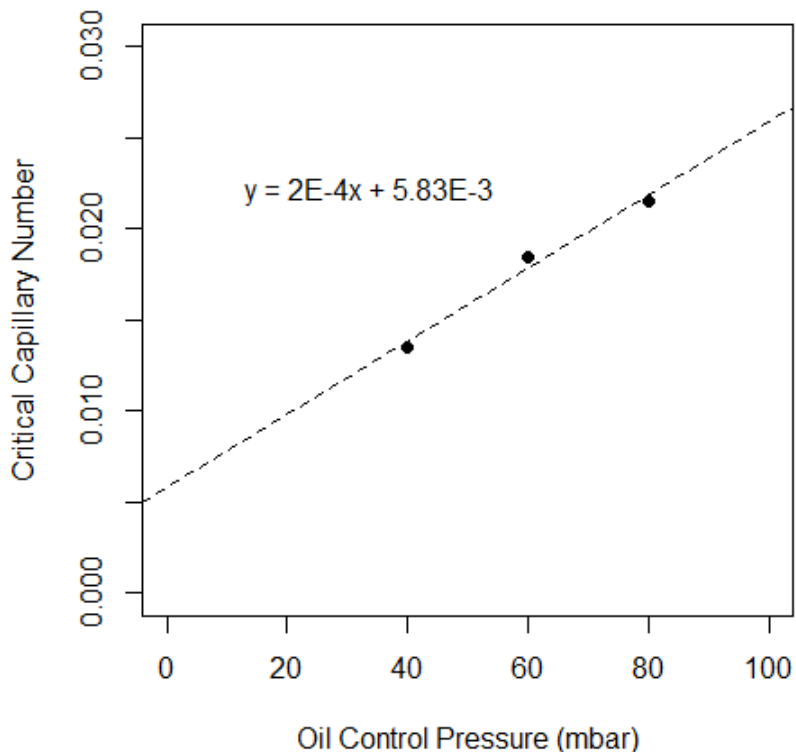


Figure 4.5: Critical capillary number as a function of continuous phase applied pressure.

The difference in critical capillary number is likely due to the use of droplet velocity as an approximation for mean continuous phase velocity. Others have surmised that

there is some numerical difference between the velocity of the droplets and the mean velocity of the continuous phase [23]. Unfortunately, due to the complex nature of multiphase flow during droplet formation it may be difficult to further investigate the true mean velocity of the continuous phase. However, a correction can be made by applying the linear relationship between the applied control pressure of the continuous phase and the critical capillary number such that the regime transition is coincident, as shown in Figure 4.6.

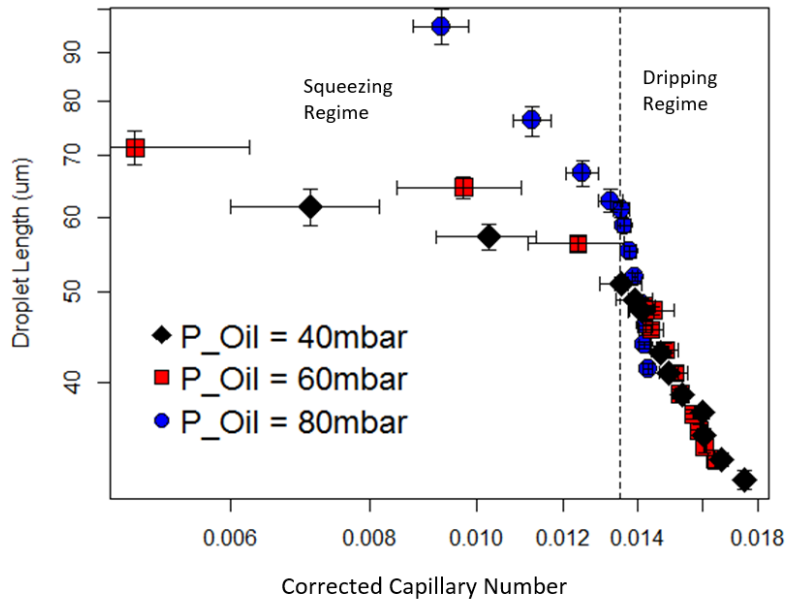


Figure 4.6: Droplet length as a function of corrected capillary number. The dashed vertical line shows the interpreted point of transition.

This interpretation of droplet length as a function of corrected critical capillary number is a simplification that clearly demonstrates the regime transition. However, it should be noted that these capillary numbers have first been approximated, then linearly scaled, and that a systematic investigation in which flowrates are calculated by varying methods should be conducted to understand the effect on capillary number approximation.

#### 4.4.2 Droplet Polydispersity

Dimensional analysis of droplet length shows there is no statistically meaningful difference in droplet length as measured at varying points as the droplet migrates down the channel. Additionally, there does not appear to be any strong trend in measured droplet length over the duration of image acquisition. Both histograms and Quantile-Quantile plots of the mean droplet length suggest the populations to be largely normal.

Polydispersity in syringe pump based systems suffers, particularly at low flow velocities, due to minor fluctuations in the stepper-motor-actuated syringe plungers [8]. Here, polydispersity is measured by the coefficient of variation (CV) on the populations droplet length. In the populations measured, the CV was below 1%. This is significantly lower than the 6 to 10% CVs reported by experimental observations in T-junctions using syringe pumps at similar flowrates [8]. The results are similar to the polydispersity reported by others using pressure-driven flow. However, the CVs shown here suggest this system is capable of marginally improved monodispersity relative to the 2% CVs reported elsewhere and at even lower flowrates [13, 16]. The lowest continuous phase flowrate droplet population measured here was 0.863  $\mu\text{L}/\text{min}$ , resulting in a capillary number of 0.010 and CV of 0.95.

# Chapter 5

## Conclusions

### 5.1 Areas of Further Investigation

Given the nature of the PDFC as a general flow provider and that it is intended to be used for applications outside of droplet formation there are systems aspects that may be improved.

#### 5.1.1 Improvement of Time Response

It may be beneficial to seek faster actuating regulators and to improve the signal propagation time (currently limited by the LabVIEW VISA tool set). One approach may be to move pressure control signal generation to the microcontroller and to use LabVIEW as a tool only to set parameters that drive specific time-dependent functions on the micro-controller. Similarly, the microcontroller could be interacted with directly, bypassing the need for LabVIEW integration all together by use of custom inputs. It is also important for future users to consider that compressibility of the system will have an impact on the response time.

#### 5.1.2 Determination of Flowrate

One of the limitations of the system is the determination of flowrates. Multiple methods of flowrate determination have been described here, including droplet velocity, mass measurement, and hydraulic resistance approximation. Each of these methods has some drawback that makes application difficult. It is conceivable that imageJ (or similar) image analysis could be used to develop a tool capable of automatically determining flowrates and would be valuable for a broad range of applications.

## 5.2 Achievements

This project was divided into two primary objectives. First, to develop and characterize a pressure driven flow controller system for use as flow provider in microfluidic applications. Second, the system was applied to the generation of droplets using a T-junction microfluidic device.

### 5.2.1 Device Development

The PDFC system was successfully integrated into the existing microfluidic laboratory set-up. The initial design inputs were all fulfilled as demonstrated by the presented system characterization. The system was shown to have a response time on the order of magnitude of approximately 1000ms, significantly faster than comparable syringe pump based systems [4]. The resulting regulated pressures were shown to be very stable with low inter-channel variation. The PDFC was measured to be capable of  $\pm 1$  mbar accuracy with a signal standard deviation of less than 0.25 mbar, and signal to noise ratio of 400. This highly stable pressure results in high stable flowrates given the system is allowed to come to steady-state, and therefore in the application of droplet formation produces high monodispersed droplets.

### 5.2.2 Application to Droplet Formation

The PDFC was subsequently used to produce droplets at low capillary numbers in T-junction micro-channels. The transition between flow regimes was established, shown in Figures 4.2 on page 23 and 4.3 on page 24. While the parameters and conditions resulting in droplet-formation regime transition have been well documented by others, this, to the best of the authors knowledge, is the first time the transition has been experimentally documented in a pressure-driven flow system. The transition was quantified by the outer capillary number, and was found to be 0.0135, 0.0185, and 0.0215 for the three different continuous phase pressures tested, similar to values previously reported [8, 11]. However, unlike previous findings the critical capillary number was not shown to be universal across multiple flow conditions. This may be due to the approximation of the continuous phase mean velocity as calculated from the measured droplet velocity.

The droplets produced were highly monodisperse in normally distributed populations, with droplet length coefficient of variations of less than 1%. This level of monodispersity was considerably improved relative to syringe pump based systems, and similar to monodispersity achieved by others using similar systems[13, 16].

# Appendix A

## Arduino Code

```
//Aaron Delahanty
//2224135D@student.gla.ac.uk
//University of Glasgow
//21Oct2015
//Electronic Flow Controller

//This application (sketch) is intended to be the sole sketch responsible for
//measuring
//and regulating pressure in the Electronic Flow Control (EFC) system being developed
//for T.Franke's microfluidic group. The objective of the sketch is to facilitate
//communication with two types of integrated chips (i) Analog Microselectronic's
//AMS5915
//pressure sensors, and (ii) Microchip Technology Inc.'s MCP4921 DAC.

//In addition to this sketch the system will use a LabView VI to set the desired
//pressure values by DAC, and display the measured pressure for the 4 discrete
//channels
//This communication will be facilitated by serial communication over USB.

//Revision Notes:
//02192016 - Removed Voltmeter functionality
//           - Removed All Delays
//           - 4th Channel DAC is faulting (output is always 1V)

//Wire.h is the arduino library for I2C/TWI comm
#include <Wire.h>
#include <SPI.h>

//Define variables used for conversion of pressure units from raw counts mbar.
int p_min;
int p_max;
int digoutp_min;
int digoutp_max;

//Define array for pressure channel comparison and final output
//Comparison is used to determine whether the high range 1000mbar or high resolution
//350mbar sensor should be used
float p_comp[8];
float p_out[4];

//Prior to sending the 12bit input which will drive the T2000 pressure regulators
//the DAC needs to receive 4 configuration bits
//Bit 15 - 0 = write to DAC, 1 = ignore command
//Bit 14 - BUF; 1 = buffer v_ref, 0 = bypass buffer
//Bit 13 - GA; 1 = v_out is 1X v_ref, 0 = vout is 2X v_ref
```

```

//Bit 12 - SHDN; 1 = active, 0 = shutdown DAC

//Default configuration bits set to [0,1,1,1]
unsigned int Config = B0111;

void setup()
{
    //Set baud rate to 9600
    Serial.begin(9600);
    // join i2c bus
    Wire.begin();
    // join SPI bus
    SPI.begin();
}

void loop()
{

//START DAC CODE:

// check serial

if ( Serial.available() ){
    // cast the string read in an integer
    String p_write = Serial.readString();

    int commaIndex1 = p_write.indexOf(',');
    int commaIndex2 = p_write.indexOf(',',commaIndex1+1);
    int commaIndex3 = p_write.indexOf(',',commaIndex2+1);

    String P1s = p_write.substring(0,commaIndex1);
    String P2s = p_write.substring(commaIndex1+1,commaIndex2);
    String P3s = p_write.substring(commaIndex2+1,commaIndex3);
    String P4s = p_write.substring(commaIndex3+1);

    unsigned int a[3];
    a[0]=P1s.toInt();
    a[1]=P2s.toInt();
    a[2]=P3s.toInt();
    a[3]=P4s.toInt();

    float cs[3];
    for (int i = 0; i <= 3; i++)
    {
        cs[i] = i+7;
        pinMode(cs[i], OUTPUT);

        //Command is the variable sent to DAC to drive pressure regulator
        //The command variable is comprised of the 4 configuration bits and 12 data
        //bits
        unsigned int command;
        //Shift the config bits 12 positions leftward, augment with the a[i] pressure
        //value
        //in volts
        command = ( Config << 12 | a[i] );

        //Write command to each ith DAQ
        SPI.beginTransaction(SPISettings(20000000, MSBFIRST, SPI_MODE0));
        //Set ith output pin to LOW, in order to accept write command
        digitalWrite(cs[i], LOW);
        //SPI.transfer function is only capable of sending 8bits at a time
        //The 16bit command is therefore split into a high and low byte
        int high = highByte(command);
        int low = lowByte(command);
    }
}
}

```

```

        SPI.transfer(high);
        SPI.transfer(low);
        SPI.endTransaction();
        //Set i'th pin HIGH to end write command
        digitalWrite(cs[i], HIGH);
        //Optional print for debugging
        //Serial.println("16bit command sent:");
        //Serial.println(value,BIN);
    }
}

//END DAC CODE

//START PRESSURE SENSOR CODE:

//Define buffer to hold sampled values
byte buffer[4];

for (int addr = 1; addr <= 8; addr++)
{
    //Pressure sensor addresses have been configured to 1 through 8.
    //Sensors 1,2,3,4 are high range 1000mbar
    if (addr <= 4)
    {
        //Set conversion constants for AMS 5915-1000-D
        p_min = 0;
        p_max = 1000;
        digoutp_min = 1638;
        digoutp_max = 14745;
    }

    //Sensors 5,6,7,8 are high resolution 350mbar
    else
    {
        //Set conversion constants for AMS 5915-350-D-B
        p_min = 0;
        p_max = 350;
        digoutp_min = 1638;
        digoutp_max = 14745;
    }

    //Wire.requestFrom(address, quantity)
    //address: the 7-bit address of the device to request bytes from
    //quantity: the number of bytes to request
    //request four bytes from sensor (first 2 are pressure, second 2 are temp)
    int n = Wire.requestFrom (addr, 4);

    //Ensure response is 4byte
    if(n == 4)
    {

        Wire.readBytes (buffer, 4);

        unsigned int p_raw = word (buffer[0], buffer[1]);      // word(high,low)
        unsigned int t_raw = word (buffer[2], buffer[3]);

        // note that the next bit operations works best with "unsigned int", not
        // with "int"
        p_raw &= 0x3FFF;      // 14bits pressure data
        t_raw >>= 5;          // 11bits temperature data, shift them in position

        // convert raw pressure to mbar (equation and constants from datasheet)
        float pressure = ((( (float) p_raw - digoutp_min ) / ((digoutp_max -
        digoutp_min) / (p_max - p_min))) + p_min );
    }
}

```

```

        // convert raw temperature to degC (equation and constants from datasheet
        )
        float temperature = (( (float) t_raw * 200.0 ) / 2048.0 ) - 50.0;

        // with the pressure comparison array with all sensor's outputs
        p_comp[addr-1] = pressure;
    }

    //If no response is present, or response is not 4bytes
    else
    {
        Serial.println ("Error, no sensor found");
    }
}

int i;
for (i = 0; i <= 3; i++)
{
    if (p_comp[i]> 350)
    {
        p_out[i] = p_comp[i];
    }
    else
    {
        p_out[i] = p_comp[i+4];
    }
    Serial.println(p_out[i]);
}
// END PRESSURE SENSOR CODE
}

```

# Appendix B

## LabVIEW VI

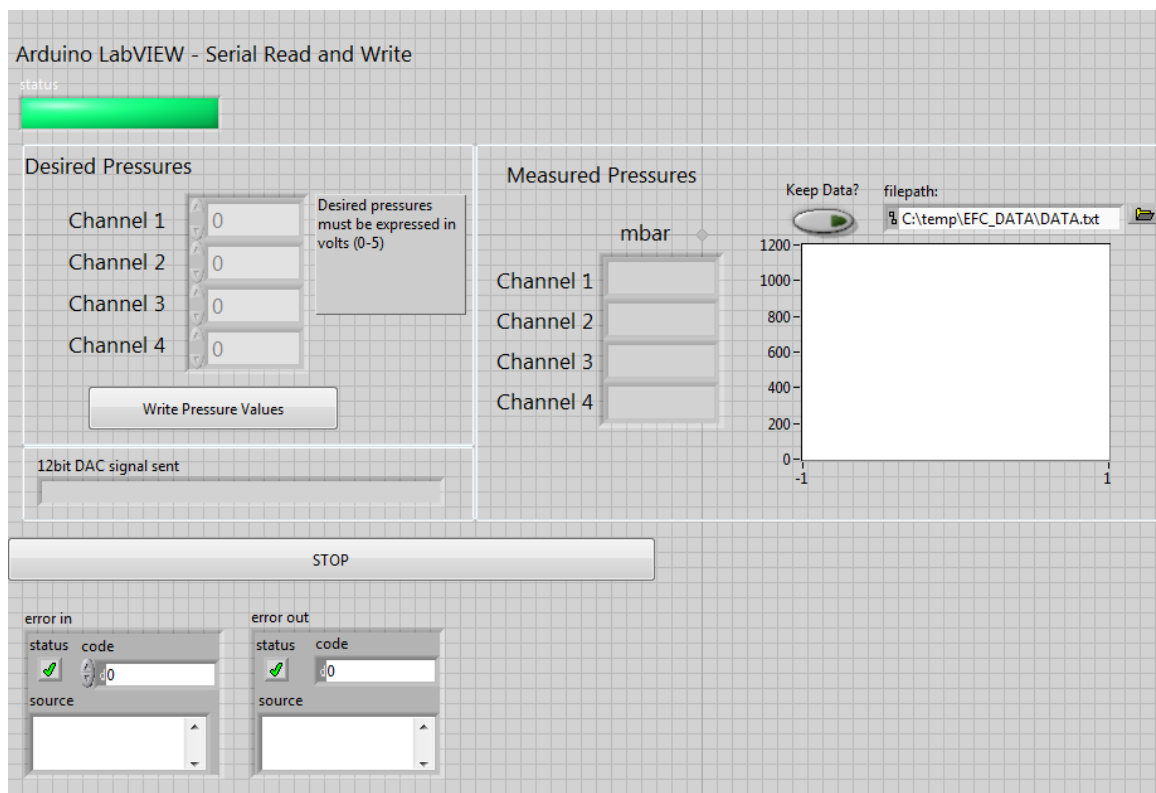


Figure B.1: LabVIEW Frontend

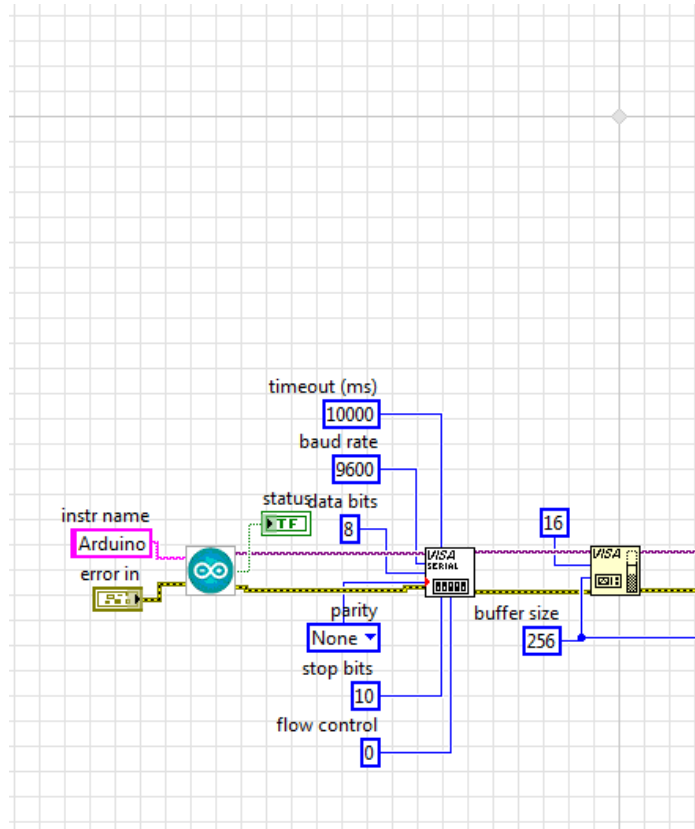


Figure B.2: LabVIEW Backend 1

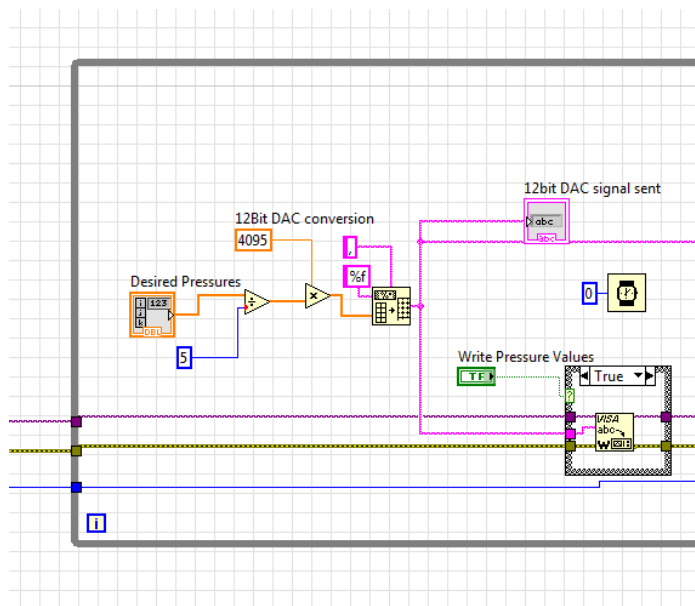


Figure B.3: LabVIEW Backend 2

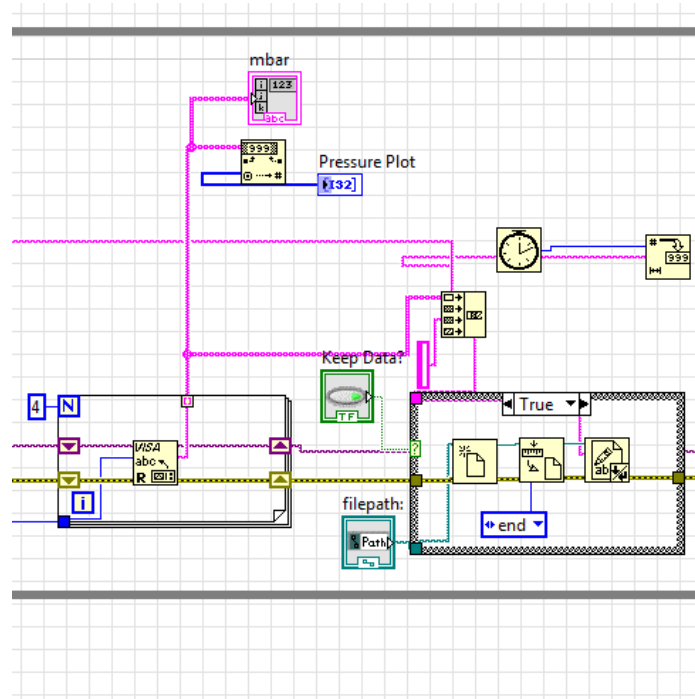


Figure B.4: LabVIEW Backend 3

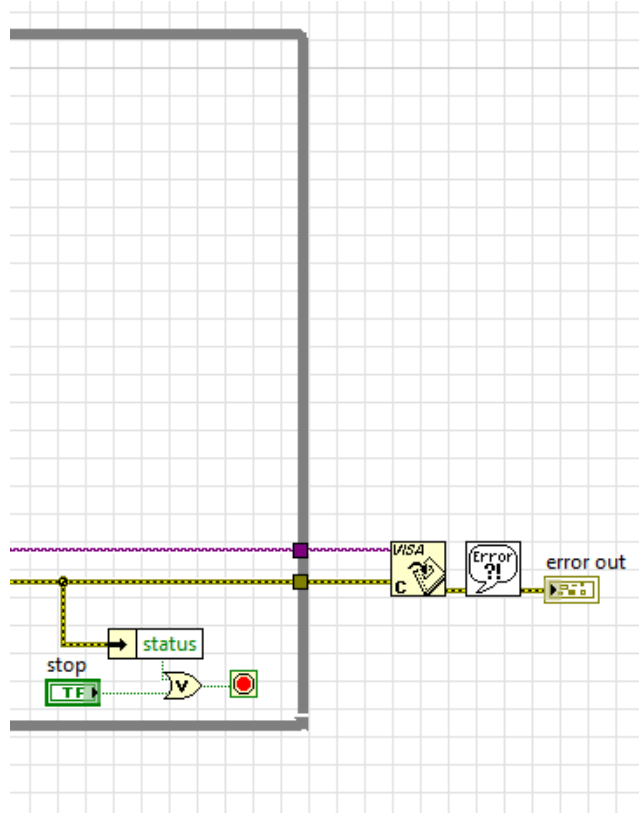


Figure B.5: LabVIEW Backend 4

# Appendix C

## Supplementary Statistics

P Oil:

40 mbar	<pre> Residuals:   1      2      3 0.08168 -0.16335 0.08168 Coefficients:             Estimate Std. Error t value Pr(&gt; t ) (Intercept) -11.089     3.114   -3.561   0.174 x            5.370     1.132    4.745   0.132  Residual standard error: 0.2001 on 1 degrees of freedom Multiple R-squared:  0.9575,    Adjusted R-squared:  0.915 F-statistic: 22.52 on 1 and 1 DF,  p-value: 0.1322 </pre>
60 mbar	<pre> Residuals:   1      2      3 -0.0124  0.0248 -0.0124 Coefficients:             Estimate Std. Error t value Pr(&gt; t ) (Intercept) -4.9966    0.4943  -10.11   0.0628 . x            4.1507    0.2578   16.10   0.0395 * --- Signif. codes:  0 '****' 0.001 '**' 0.01 '*' 0.05 '.' 0.1 ' ' 1 Residual standard error: 0.03038 on 1 degrees of freedom Multiple R-squared:  0.9962,    Adjusted R-squared:  0.9923 F-statistic: 259.3 on 1 and 1 DF,  p-value: 0.03948 </pre>
80 mbar	<pre> Residuals:   1      2      3 -0.01414  0.02829 -0.01414 Coefficients:             Estimate Std. Error t value Pr(&gt; t ) (Intercept) -3.2487    0.5883  -5.522   0.1140 x            3.9089    0.3920   9.972   0.0636 . --- Signif. codes:  0 '****' 0.001 '**' 0.01 '*' 0.05 '.' 0.1 ' ' 1  Residual standard error: 0.03465 on 1 degrees of freedom Multiple R-squared:  0.99,    Adjusted R-squared:  0.9801 F-statistic: 99.45 on 1 and 1 DF,  p-value: 0.06362 </pre>

Figure C.1: Linear Regression Statistical Summary for linear fit to L/W as a function of applied pressure ratios.

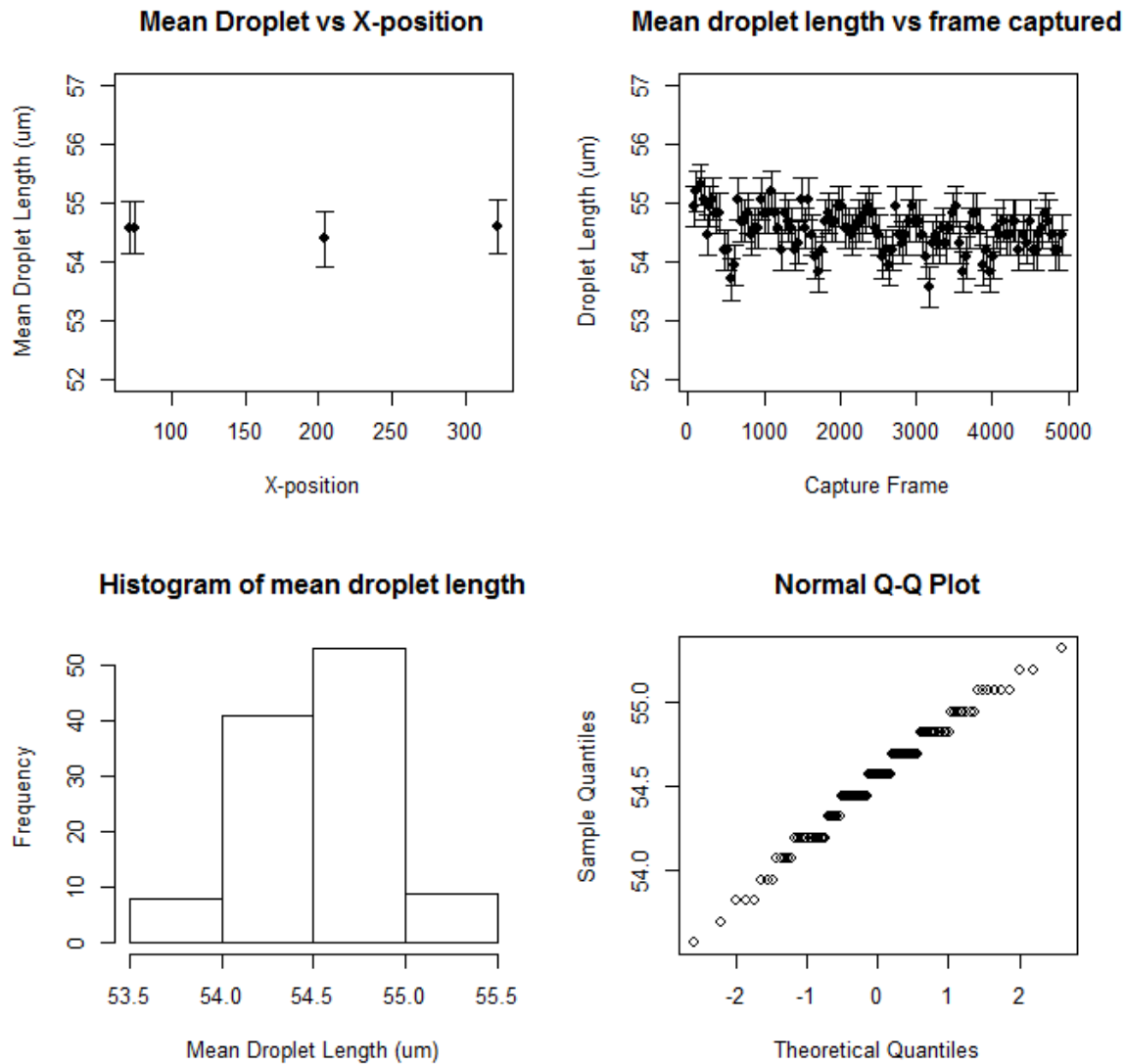


Figure C.2: Polydispersity at CA = 0.014

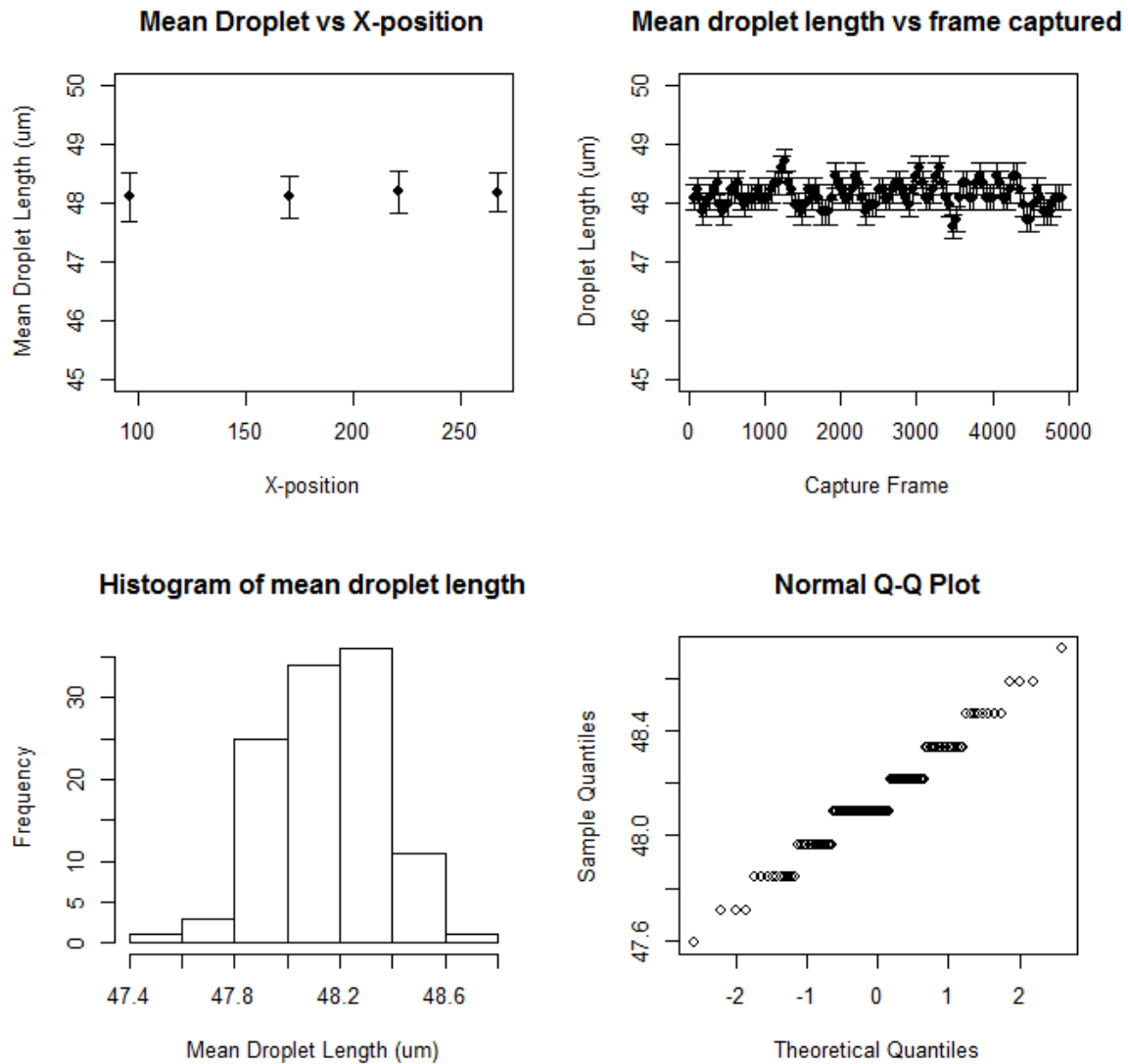


Figure C.3: Polydispersity at CA = 0.018

# Bibliography

- [1] 3M. 3M Novec 7200 Engineered Fluid. Datasheet, 2009.
- [2] Adam R. Abate, Pascaline Mary, Volkert van Steijn, and David A. Weitz. Experimental validation of plugging during drop formation in a T-junction. *Lab on a Chip*, 12(8):1516, 2012.
- [3] Charles N. Baroud, Francois Gallaire, and Rémi Dangla. Dynamics of microfluidic droplets. *Lab on a Chip*, 10(16):2032, 2010.
- [4] Ki Wan Bong, Stephen C Chapin, Daniel C Pregibon, David Baah, Tamara M Floyd-Smith, and Patrick S Doyle. Compressed-air flow control system. *Lab on a chip*, 11(4):743–7, 2011.
- [5] Henrik Bruus. *Theoretical microfluidics*, volume 18. Oxford ; New York : Oxford University Press, 2008., 2008.
- [6] Lorenzo Capretto, Wei Cheng, Martyn Hill, and Xunli Zhang. Micromixing within microfluidic devices. *Topics in Current Chemistry*, 304(1):27–68, 2011.
- [7] Zhuang Zhi Chong, Say Hwa Tan, Alfonso M Ganan-Calvo, Shu Beng Tor, Ngiap Hiang Loh, and Nam-Trung Nguyen. Active droplet generation in microfluidics. *Lab Chip*, 16:35–58, 2016.
- [8] Gordon F. Christopher, N. Nadia Noharuddin, Joshua A. Taylor, and Shelley L. Anna. Experimental observations of the squeezing-to-dripping transition in T-shaped microfluidic junctions. *Physical Review E - Statistical, Nonlinear, and Soft Matter Physics*, 78(3), 2008.
- [9] Krzysztof Churski, Michal Nowacki, Piotr M. Korczyk, and Piotr Garstecki. Simple modular systems for generation of droplets on demand. *Lab on a Chip*, 13(18):3689–3697, 2013.
- [10] Vittorio Cristini and Yung-Chieh Tan. Theory and numerical simulation of droplet dynamics in complex flows-a review. *Lab on a Chip*, 4(4):257–264, 2004.
- [11] M. De Menech, P. Garstecki, F. Jousse, and H. a. Stone. Transition from squeezing to dripping in a microfluidic T-shaped junction. *Journal of Fluid Mechanics*, 595:141–161, 2008.
- [12] Piotr Garstecki, Michael J. Fuerstman, Howard A. Stone, and George M. Whitesides. Formation of droplets and bubbles in a microfluidic T-junctionscaling and mechanism of break-up. *Lab on a Chip*, 6(3):437, 2006.
- [13] Tomasz S Kaminski, Ott Scheler, and Piotr Garstecki. Droplet microfluidics for microbiology: techniques, applications and challenges. *Lab Chip*, 16:2168–2187, 2016.
- [14] Clement Kleinstreuer. *Microfluidics and Nanofluidics: Theory and Selected Applications: Theory and Selected Applications*. 2013.
- [15] Zida Li, Sze Yi Mak, Alban Sauret, and Ho Cheung Shum. Syringe-pump-induced fluctuation in all-aqueous microfluidic system implications for flow rate accuracy. *Lab on a Chip*, 14(4):744, 2014.
- [16] Jiseok Lim, Ouriel Caen, Jérémie Vrignon, Manfred Konrad, Valérie Taly, and Jean Christophe Baret. Parallelized ultra-high throughput microfluidic emulsifier for multiplex kinetic assays. *Biomicrofluidics*, 9(3), 2015.
- [17] Lothar Schmid and Thomas Franke. Acoustic modulation of droplet size in a T-junction. *Applied Physics Letters*, 104(13):133501 p.1–4, 2014.
- [18] Lingling Shui, J. C T Eijkel, and Albert van den Berg. Multiphase flow in micro- and nanochannels. *Sensors and Actuators, B: Chemical*, 121(1):263–276, 2007.

- [19] Lingling Shui, Jan C T Eijkel, and Albert van den Berg. Multiphase flow in microfluidic systems - Control and applications of droplets and interfaces. *Advances in Colloid and Interface Science*, 133(1):35–49, 2007.
- [20] H A Stone, A D Stroock, and A Ajdari. ENGINEERING FLOWS IN SMALL DEVICESMicrofluidics Toward a Lab-on-a-Chip. *Annual Review of Fluid Mechanics*, 36(1):381–411, 2004.
- [21] A.D. Stroock and G.M. Whitesides. Components for integrated poly (dimethylsiloxane) microfluidic systems. *Electrophoresis*, 23(20):3461–3473, 2002.
- [22] Todd Thorsen, Richard W. Roberts, Frances H. Arnold, and Stephen R. Quake. Dynamic pattern formation in a vesicle-generating microfluidic device. *Physical Review Letters*, 86(18):4163–4166, 2001.
- [23] Thomas Ward, Magalie Faivre, Manouk Abkarian, and Howard A. Stone. Microfluidic flow focusing: Drop size and scaling in pressure versus flow-rate-driven pumping. *Electrophoresis*, 26(19):3716–3724, 2005.
- [24] Jian Hong Xu, S. W. Li, J. Tan, and G. S. Luo. Correlations of droplet formation in T-junction microfluidic devices: From squeezing to dripping. *Microfluidics and Nanofluidics*, 5(6):711–717, 2008.